doi.org/10.26434/chemrxiv.7684043.v1

Mechanochemistry Enables Targeted Synthesis of Mixed-Metal Microporous Metal-Organic Frameworks Using Pre-Assembled Precursors

Ghada Ayoub, Bahar Karadeniz, Ashlee J. Howarth, Omar Farha, Ivica Đilović, Luzia S. Germann, Robert E. Dinnebier, Krunoslav Užarević, Tomislav Friscic

Submitted date: 06/02/2019 • Posted date: 07/02/2019

Citation information: Ayoub, Ghada; Karadeniz, Bahar; Howarth, Ashlee J.; Farha, Omar; Đilović, Ivica; Germann, Luzia S.; et al. (2019): Mechanochemistry Enables Targeted Synthesis of Mixed-Metal Microporous Metal-Organic Frameworks Using Pre-Assembled Precursors. ChemRxiv. Preprint.

Ball milling mechanochemistry enables enables targeted, rapid synthesis of mixed-metal metal-organic frameworks (MOFs) with controllable stoichiometric composition. Specifically, the use of ball milling enabled the use of pre-assembled coordination polymers of zinc, magnesium, nickel(II) and cobalt(II) as precursors in an innovative mechanochemical strategy for the deliberate assembly of mixed-metal MOF-74 materials comprised of pairs of transition of main group metals in a pre-determinmed 1:1 stoichiometric ratio, including ZnMg-, ZnCo, ZnCu, MgZn-, MgCo-, MgCa-, NiZn-,NiMg-, NiCo-, CoZn-, CoMg- and CoCu-MOF-74. While this is the first example of target-oriented MOF synthesis using mechanochemistry, it also provides an entry to controlling the stoichiometric composition of mixed-metal frameworks.

File list (2)

Mechanochemistry enables targeted synthesis of mixed-metal microporous metal-organic frameworks using pre-assembled precursors

Ghada Ayoub,[a] Bahar Karadeniz,[b] Ashlee J. Howarth,[c,d] Omar K. Farha*,[c] Ivica Đilović,[e] Luzia S. Germann,[f] Robert E. Dinnebier,[f] Krunoslav Užarević*,[b] Tomislav Friščić[a,b]*

[a]Department of Chemistry, McGill University, 801 Sherbrooke Street W, Montreal, QC, H3A 0B8, Canada; [b]Institute Ruđer Bošković, Bijenička 54, HR-10000 Zagreb, Croatia; [c]Department of Chemistry, Northwestern University, 2145 Sheridan Rd, Evanston, IL 60208, USA; [d]Department of Chemistry & Biochemistry, Concordia University, Montreal, H4B 1R6, Canada. [e]Department of Chemistry, Faculty of Science, Zagreb 10000, Croatia; [f]Max Planck Institute for Solid-State Research, Stuttgart 70569, Germany.

Abstract

Ball milling mechanochemistry enables targeted, rapid synthesis of mixed-metal metal–organic frameworks (MOFs) with controllable stoichiometric composition. Specifically, the use of ball milling enabled the use of pre-assembled coordination polymers of zinc, magnesium, nickel(II) and cobalt(II) as precursors in an innovative mechanochemical strategy for the deliberate assembly of mixed-metal MOF-74 materials comprised of pairs of transition or main group metals in a pre-determined 1:1 stoichiometric ratio, including ZnMg-, ZnCo-, ZnCu-, MgZn-, MgCo-, NiZn-, NiMg-, NiCo-, CoZn-, CoMg-, CoCu-, and MgCa-MOF-74. While this is the first example of target-oriented MOF synthesis using mechanochemistry, it also provides an entry to controlling the stoichiometric composition of mixed-metal frameworks.

Introduction

Metal-organic frameworks (MOFs) are a class of robust network materials made up of organic linkers and metal-based nodes.[1-5] Outstanding properties of MOFs, such as high surface areas,[6-8] accessible pores of tunable size,[9-12] or open metal sites[13-15] make them attractive diverse applications, *e.g.* gas storage, separation,[16-23] catalysis,[24-27] sensing,[28-30] magnetism,[31-33] drug delivery,[34-36] *etc*. Mixed-metal MOFs, involving nodes based on two or more different metals, are becoming increasingly attractive as a means to achieve materials of increased complexity and functionality.[37-42] The MOF-74 class of materials[43-45] has been of particular interest due to modular design, stability, as well as accessibility of open metal sites. These materials are typically built from divalent metal nodes (M= Zn, Mg, Ni, Cu, Co, Cd, *etc.*) involved in rod secondary building units (SBUs) cross-linked by bridging dicarboxylate ligands into a honeycomb-like structure with pore diameters ≈12 Å.[46] Recent studies have shown an increase in adsorption, stability, and catalytic activity of MOF-74 achieved by the partial incorporation of hetero-metal nodes into the MOF-74 architecture.[47,48] While the MOF-74 architecture is particularly amenable for the synthesis of mixed-metal framework materials, the control of the stoichiometric composition and distribution of metal centers in such materials remains a challenge (Fig. 1).[49-52]

Here, we present an efficient, mechanochemistry-based strategy for the synthesis of microporous MM'-MOF74 materials containing pairs of the divalent main group (Mg^{2+}, Ca^{2+}) or *d*-block metal cations (Co^{2+}, Ni^{2+}, Cu^{2+}, Zn^{2+}) in a reaction-controlled 1:1 stoichiometric ratio. This strategy is reliant on mechanochemical milling[53] which enables the use of well-defined discrete or polymeric metal–organic complexes as precursors.

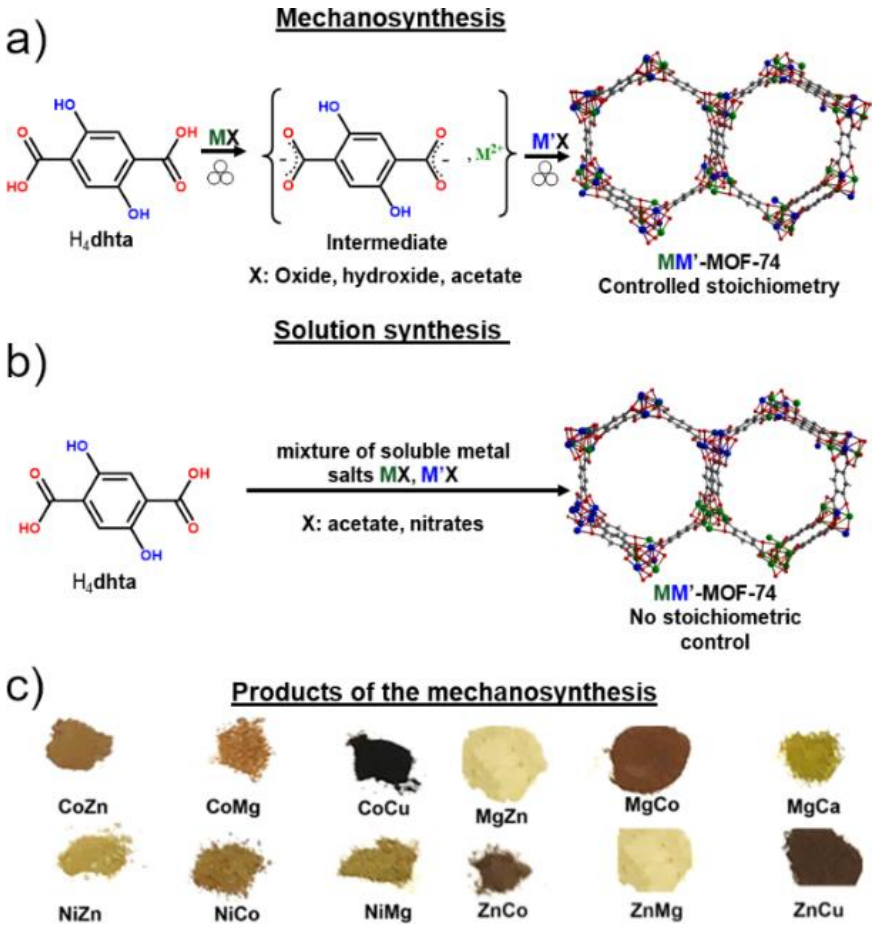

Figure 1. The difference in the synthetic routes and final products of MM'-MOF-74 in a) solid-state synthesis and b) solution synthesis. c) Optical images illustrating the appearance of the end products for the different bimetallic MM'-MOF-74 materials obtained by combination of Mg^{2+}, Ca^{2+}, Co^{2+}, Ni^{2+}, Cu^{2+}, and Zn^{2+}.

By using a solid precursor specifically prepared to assemble with a secondary metal source to form a MOF-74 structure, this approach expands on the "crystals as molecules" concept to enable a streamlined, target-oriented synthesis of a mixed-metal MOF target.[54] The herein presented strategy relies on the observation that the synthesis of zinc-based MOF-74[55] from ZnO and 2,5-dihydroxyterephthalic acid (H_4**dhta**) by milling proceeds in two stages: 1) initial formation of the coordination polymer $[Zn(H_2O)_2(H_2$**dhta**$)]_n$ (**1**) by liquid-assisted grinding (LAG)[56,57] with water, and 2) reaction of **1** with remaining ZnO to form Zn-MOF-74. The formation of **1** as a reaction intermediate was explained by higher reactivity of H_4**dhta** carboxylic acid groups compared to *o*-hydroxyl moieties. In principle, this two-step reaction should be applicable for the targeted synthesis of a range of mixed-metal MOF-74 derivatives from designed coordination compounds based on H_2**dhta**$^{2-}$ anions.

We now demonstrate a general, targeted approach for the synthesis of bimetallic MOF-74 materials involving different combinations of Zn^{2+}, Mg^{2+}, Co^{2+}, Ni^{2+}, Cu^{2+} and Ca^{2+} by mechanochemical reaction of predesigned intermediate complexes **1**, $Mg(H_2O)_5(H_2$**dhta**$)\cdot H_2O$ (**2**), $[Ni(H_2O)_4(H_2$**dhta**$)\cdot 2H_2O]_n$ (**3**) and $[Co(H_2O)_4(H_2$**dhta**$)\cdot 2H_2O]_n$ (**4**) with suitable metal oxides or acetates (Fig. 2). Importantly, using oxides and acetates as a metal source is an environmentally-friendly alternative to conventional synthesis of MOFs that often requires toxic and corrosive metal precursors such as chloride and nitrates.

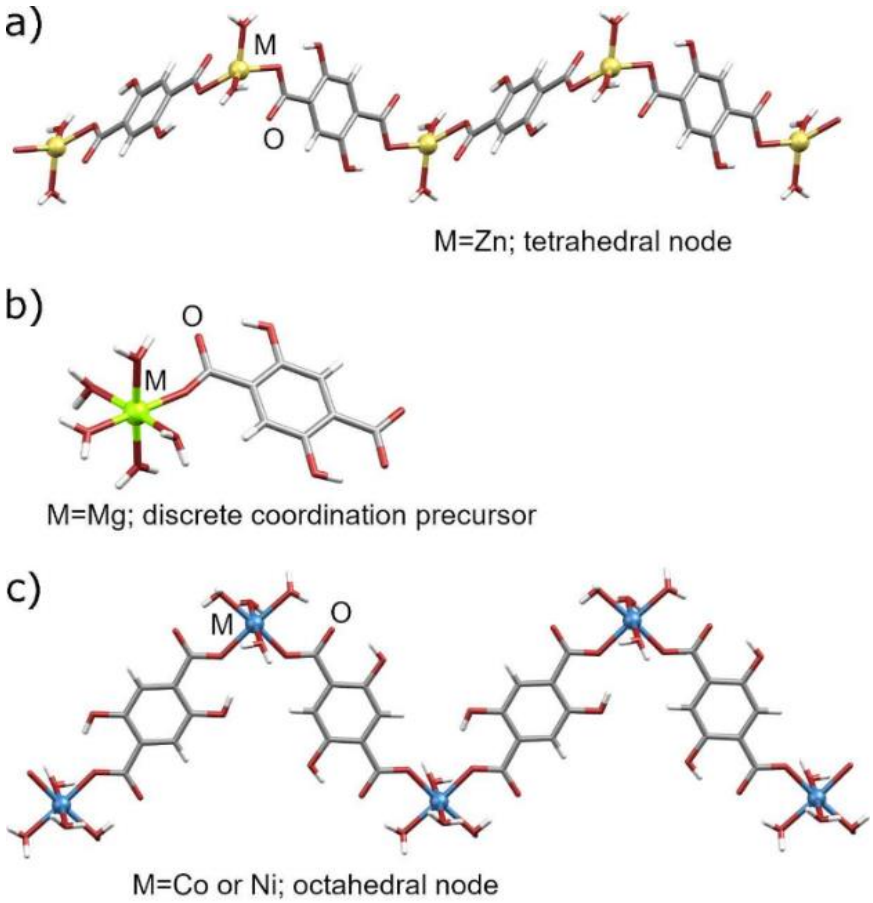

Figure 2. Crystal structure of the reactive intermediates prepared by milling stoichiometric amounts of H_4**dhta** with a metal salt to generate a) Zn (yellow), b) Mg (green), and c) Ni or Co (blue) coordination compounds.

Compounds **1-4** are readily obtained by LAG of a metal source (ZnO, MgO, $Ni(CH_3COO)_2{\cdot}4H_2O$ or $Co(CH_3COO)_2{\cdot}4H_2O$) with H_4**dhta** in one step. Structures of **1** and **2** were previously reported,[58,59] while the structures of **3** and **4** are determined here using single crystal and powder X-ray diffraction (PXRD) data, respectively (see SI).
We first explored our strategy by using **1** as a precursor in a set of LAG mechanochemical reactions involving an equimolar amount of either MgO, $CoCO_3$ or $Cu(OH)_2$. In each case, 60 minutes of milling with **1** in presence of MeOH (liquid-to-solid ratio η= 0.90 μL/mg, 0.90 μL/mg, and 0.95 μL/mg) led to the formation of MM'-MOF-74 structures, as evidenced by PXRD analysis (Fig. 3).

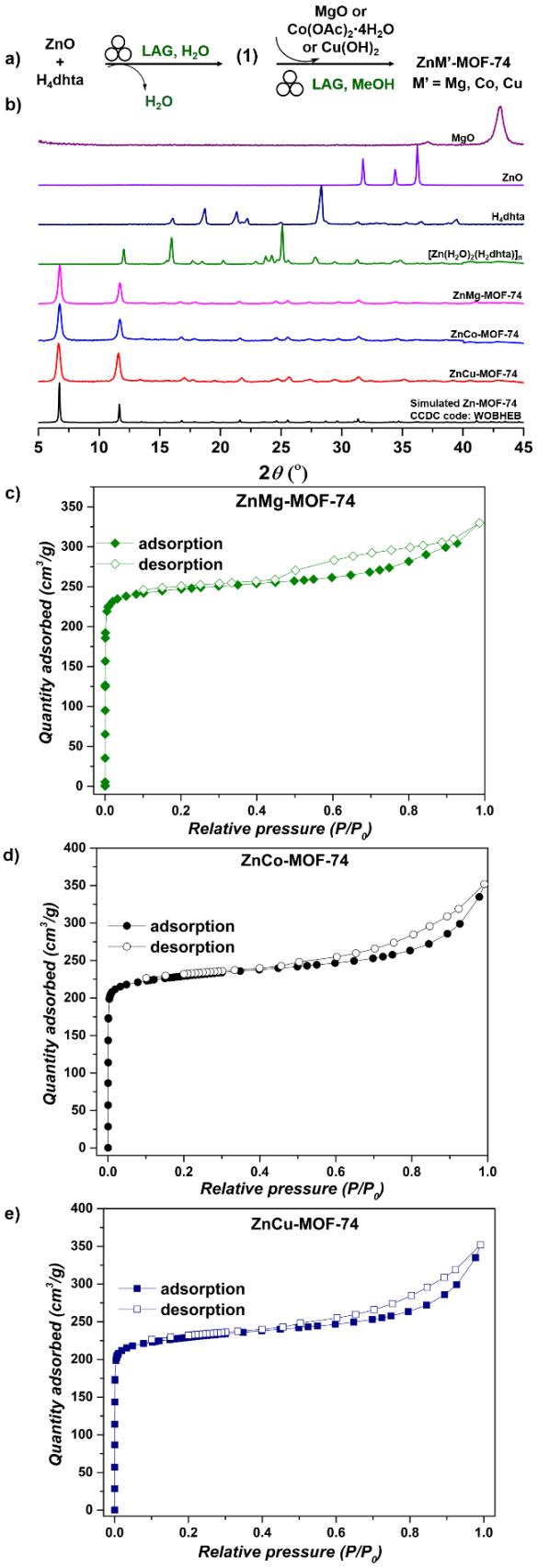

Figure 3. a) Stepwise synthesis of ZnM'-MOF-74 enabled by LAG, b) PXRD patterns of selected reactants, **1** and the mixed-metal ZnM'-MOF-74 products, compared to simulated pattern of the parent Zn-MOF-74. Nitrogen isotherms of: c) ZnMg-MOF-74, d) ZnCo-MOF-74, and e) ZnCu-MOF-74.

After washing with MeOH and activation (see SI), the resulting ZnMg-MOF-74, ZnCo-MOF-74 and ZnCu-MOF-74 exhibited Brunauer–Emmett–Teller (BET) surface areas of 1080 m^2/g, 1130 m^2/g and 910 m^2/g, respectively, calculated from N_2 isotherms measured at 77 K. Stoichiometric compositions of the materials were verified by inductively coupled plasma atomic emission spectroscopy (ICP-AES), which revealed the ratios of Zn to M' of 1.04:1 (ZnMg-MOF-74), 0.95:1 (for ZnCo-MOF-74) and 0.90:1 (for ZnCu-MOF-74).
Next, the synthesis of Mg-based MgM'-MOF-74 materials was achieved using discrete coordination complex **2** as a precursor (Figure 4a).

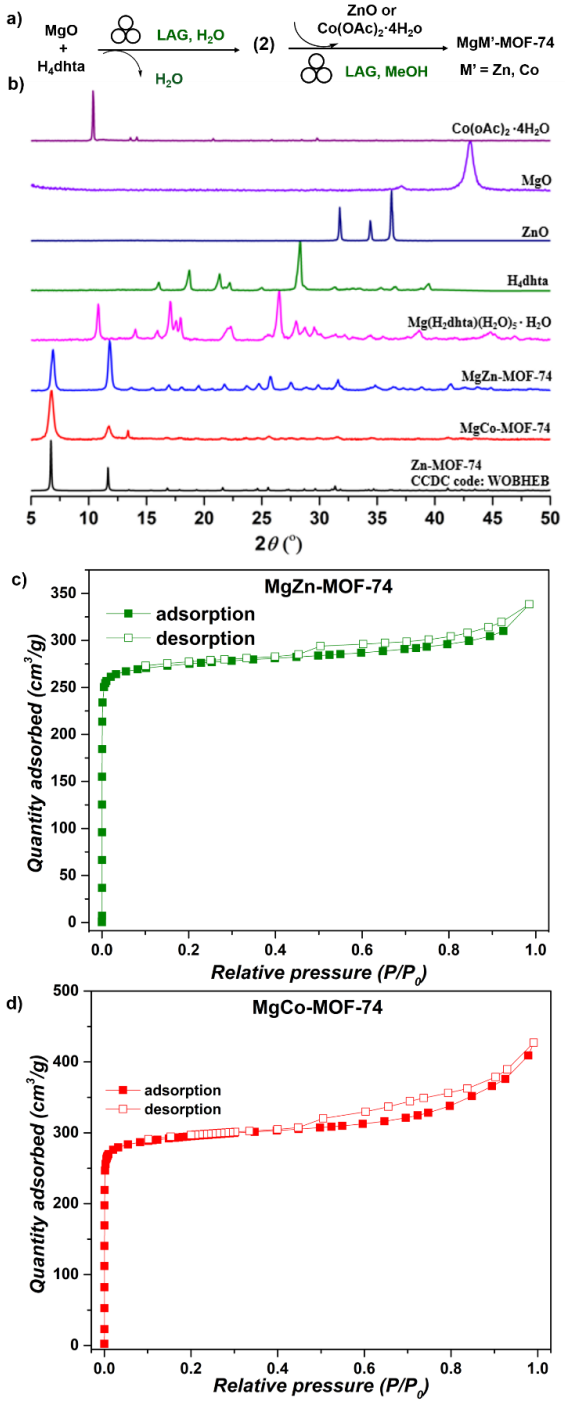

Figure 4. a) Stepwise synthesis of MgM'-MOF-74 by LAG, b) PXRD patterns of selected reactants, **2** and MgM'-MOF-74 products, compared to simulated pattern of parent Zn-MOF-74. Nitrogen isotherms of: c) MgZn-MOF-74 and d) MgCo-MOF-74.

Compound **2** was readily obtained by LAG (10 minutes) using equimolar amounts of MgO with H_4**dhta** in presence of water (η= 0.95 µL/mg and 0.85 µL/mg for MgZn- and MgCo-MOF-74, respectively). Complete conversion to **2** was evidenced by PXRD patterns measured for the milled reaction mixture exhibiting Bragg reflections consistent with the known crystal structure of **2** (CSD code XAJGEX),[58] and lack reflections for any of the reactants (Fig. 4). Subsequent milling of **2** with either ZnO or $CoCO_3$ led to the formation of MgZn-MOF-74 and MgCo-MOF-74, as evidenced by PXRD patterns obtained for the milled reaction mixtures exhibiting only reflections consistent with those of MOF-74 (Fig. 4). After washing with MeOH and subsequent activation (see SI), the MgZn-MOF-74 and MgCo-MOF-74 exhibited BET surface areas of 1100 m^2/g and 1170 m^2/g, respectively (Fig. 4). The 1:1 stoichiometric ratio of the two metals in MgCo-MOF-74 (Mg:Co ratio: 1.11:1) and MgZn-MOF-74 (Mg:Zn ratio: 1.30:1), prepared mechanochemically, was confirmed by ICP-AES.

The ability to synthesize magnesium-containing MM'-MOF-74 systems from **2** is not limited only to 1st-row *d*-block metals as components. As evidenced by PXRD (Fig. 5), milling of **2** with CaO leads to a MOF-74 structure and the disappearance of starting materials, consistent with the formation of a mixed-metal framework, MgCa-MOF-74. The formation of MgCa-MOF-74 is particularly notable due to the larger radius and coordination number of Ca^{2+} compared to Mg^{2+}. This is consistent with the surface area and ICP-AES analyses after the material has been washed with MeOH and evacuated, which revealed a surface area of 770 m^2/g (see SI) and an Mg:Ca ratio of 3:2, suggesting partial degradation and leaching of Ca^{2+} upon washing. Nevertheless, the herein prepared MgCa-MOF-74 provides the highest calcium content reported so far for a microporous MOF-74 material.

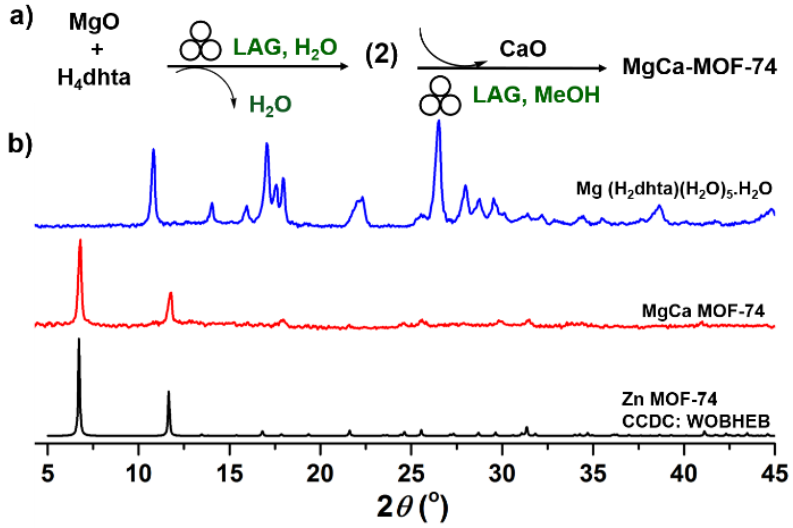

Figure 5. a) Stepwise synthesis of MgCa-MOF-74 enabled by LAG and b) the PXRD patterns of Mg coordination complex, MgCa-MOF-74 and the simulated pattern of Zn-MOF-74.

The ability to synthesize MM'-MOF-74 materials from either **1** and **2** is notable since the two reactants exhibit very different structures: while **1** is a linear coordination polymer, **2** is a discrete complex. Next, we explored transition-metal complexes **3** and **4** as a source of H_2**dhta**$^{2-}$. Both were synthesized by milling either nickel(II) or cobalt(II) acetate tetrahydrate with one equivalent of H_4**dhta**. Analysis by PXRD revealed, in both cases, the disappearance of reactants and formation of a new crystalline product. Products of the two reactions were isostructural, which is not uncommon for complexes of Co(II) and Ni(II). Single crystals of **3** were obtained from aqueous solution and X-ray analysis revealed it is a coordination polymer

similar to **1**, but based on Ni^{2+}-ions octahedrally coordinated with four water molecules and two H_2**dhta**$^{2-}$ (Figure 2c). Unlike **1**, the H_2**dhta**$^{2-}$ ligands in **3** adopt a *cis*-arrangement around each metal ion, leading to a zigzag geometry of the coordination polymer (see SI). For the synthesis of NiM'-MOF-74 materials, **3** was milled with one equivalent of either ZnO, MgO or $CoCO_3$. The formation of NiZn-, NiMg-, and NiCo-MOF-74 was confirmed by PXRD analysis of the milled reaction mixtures, which revealed only Bragg reflections consistent with a MOF-74 structure (Fig. 6). After activation, NiZn-, NiMg-, and NiCo-MOF-74 exhibited BET areas of: 1010, 860, and 870 m^2/g, calculated from N2 sorption isotherms at 77 K (see SI). The stepwise mechanosynthesis of nickel-based MM'-MOF-74 materials is readily observed by the color of the reaction mixture: initial color of the physical mixture of reactants is yellowish, which after 45 minutes converts to the pale-green color of **3** and, after milling with $CoCO_3$, ZnO or MgO converts to light brown (for NiCo-MOF-74) or pale-yellow (for NiZn- or NiMg-MOF-74) (Fig. 1). The 1:1 stoichiometric ratio of nickel to either zinc (Ni:Zn ratio: 1.06:1), magnesium (Ni:Mg ratio: 1.2:1) or cobalt (Ni:Co ratio: 1.3:1) in the MOFs was confirmed by ICP-AES.

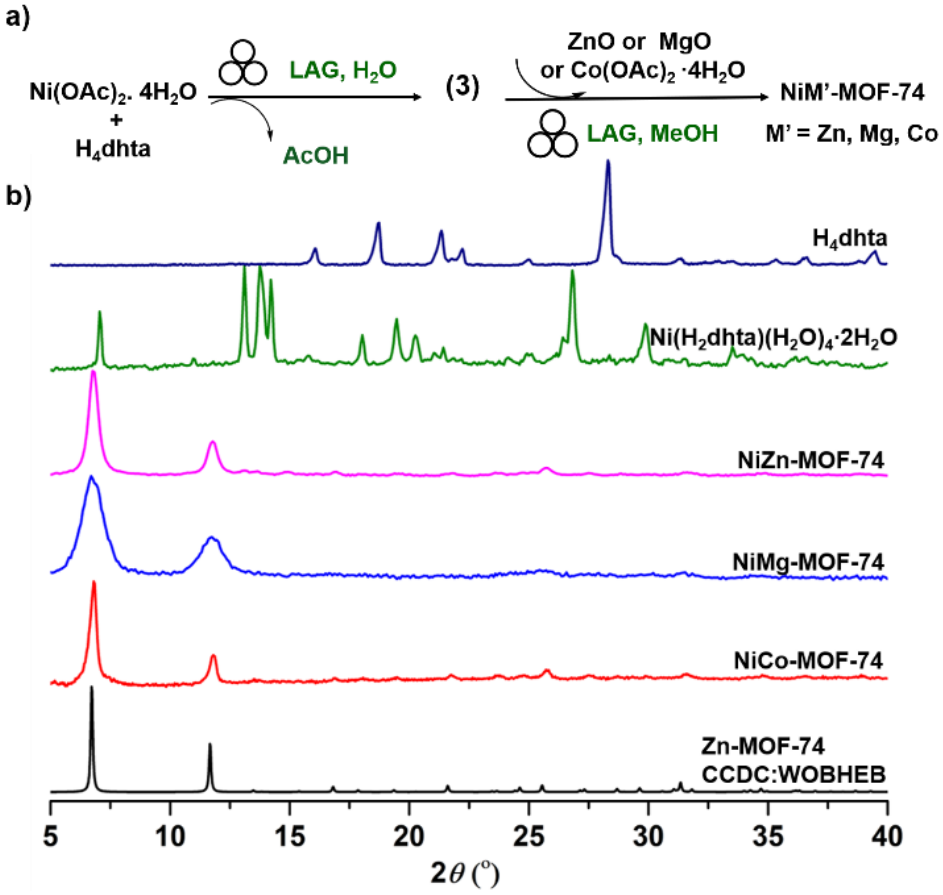

Figure 6. a) Stepwise synthesis of NiM'-MOF-74 enabled by LAG, b) PXRD patterns of the starting material, [Ni(H_2**dhta**)(H_2O)$_4$.2H_2O]n and the mixed-metal MOF-74 formed with Zn^{2+}, Mg^{2+}, and Co^{2+} sources compared to the simulated pattern of the parent Zn-MOF-74.

Attempts to obtain diffraction-quality single crystals of **4** were unsuccessful, and the structure of this material was elucidated by Rietveld refinement of the PXRD data using the isostructural **3** as starting model. Similar to **1-3**, compound 4 readily reacted with other metal sources by LAG with MeOH, providing CoM'-MOF-74 (Fig. 7). Specifically, CoZn-MOF-74, CoMg-MOF-74, and CoCu-MOF-74 were obtained by LAG of **4** with stoichiometric amounts of ZnO,

MgO, or $Cu(OH)_2$, respectively. Formation of MOF-74 structures was verified by PXRD analysis, which also revealed the absence of X-ray reflections of starting materials in the milled reaction mixtures. Analysis of metal content by ICP-AES confirmed the 1:1 ratio of cobalt to either zinc (Co:Zn ratio: 1.16:1), magnesium (Co:Mg ratio: 1.12:1) or copper (Co:Cu ratio: 1.07:1). All three mixed-metal MOFs were microporous, as shown by BET surface areas after activation of 1130 m^2/g (CoZn-MOF-74), 1315 m^2/g (CoMg-MOF-74), and 820 m^2/g (CoCu-MOF-74) (see SI).

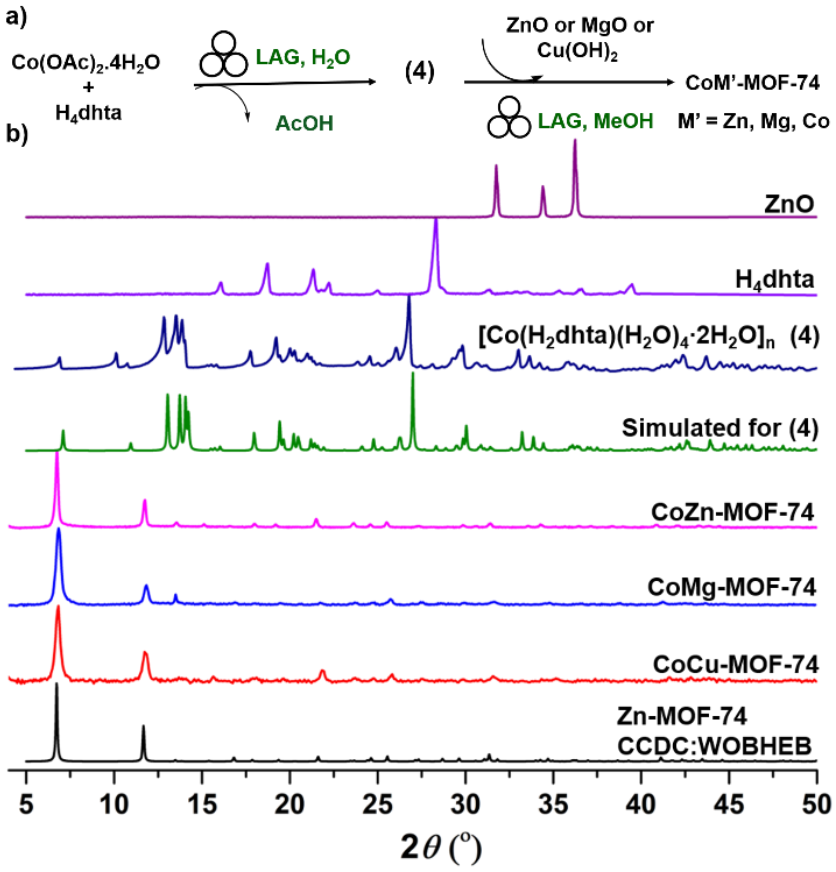

Figure 7. a) Stepwise synthesis of CoM'-MOF-74 by LAG, b) PXRD patterns of selected reactants, **4** (experimental and simulated), and CoM'-MOF-74 products, compared to the simulated powder pattern of the parent Zn-MOF-74.

In summary, we have demonstrated how mechanochemistry offers a route for targeted, efficient synthesis of microporous binary mixed-metal MOF-74 frameworks based on either transition or main group elements, with a 1:1 stoichiometric ratio of different metal nodes dictated by reaction design. In particular, mechanochemistry provides an opportunity, that is still challenging using solution-based chemistry, based on harnessing predesigned coordination complexes or polymers as a well-defined precursor for the targeted synthesis of mixed-metal MOF-74 materials with controlled stoichiometric composition of metal nodes, and starting from safe, environmentally friendly and readily accessible metal sources such as acetates, oxides, and carbonates. This mechanochemical strategy provides a rapid, simple and solvent-free approach to unique MOF-74 materials based on diverse binary combinations of metals, including lightweight nodes such as Mg^{2+}, environmentally-benevolent and biocompatible nodes such as Mg^{2+} or Ca^{2+}, as well as metal nodes of potential interest due to their catalytic or magnetic properties, such as Cu^{2+}, Ni^{2+}, or Co^{2+}, while maintaining excellent control over

metal stoichiometry. We believe this approach can be adjusted and utilized for preparation of other mixed metal MOFs based on ditopic ligands. Our following study includes determining the physico-chemical and catalytic properties of these unique bimetallic MOF-74 materials.

Additional details on experimental procedures and instrumental techniques. Crystallographic data in CIF format for crystal structures of 3 and 4. This data has been deposited with the Cambridge Crystallographic Data Centre under deposition codes 1893479 and1894933. Additional characterization data, including infrared spectra, nitrogen sorption isotherms, electron microscopy images, and thermogravimetric analysis data. The Supporting Information is available free of charge on the ACS Publications website.

Acknowledgment
We acknowledge the support of NSERC Discovery Grant (RGPIN-2017-06467) and E. W. R. Steacie Memorial Fellowship (SMFSU 507347-17). O.K.F. gratefully acknowledges support from the Defense Threat Reduction Agency (HDTRA1-18-1-0003).

References
1. Li, H.; Eddaoudi, M.; O'Keeffe, M.; Yaghi, O. M., Design, and synthesis of an exceptionally stable and highly porous metal-organic framework. *Nature* **1999,** *402*, 276-279.
2. Férey, G. Hybrid porous solids: past, present, future. *Chem. Soc. Rev*., **2008**, *37*, 191-214.
3. Horike, S.; Shimomura, S.; Kitagawa, S. Soft porous crystals. *Nat. Chem*., **2009**, *1*, 695-704.
4. Evans, J. D.; Huang, D. M.; Hill, M. R.; Sumby, C. J.; Sholl, D. S.; Thornton, A. W.; Doonan, C. J. Molecular Design of Amorphous Porous Organic Cages for Enhanced Gas Storage. *J. Phys. Chem. C* **2015**, *119*, 7746-7754.
5. Bennett, T. D.; Cheetham, A. K. Amorphous Metal–Organic Frameworks. *Acc. Chem. Res.* **2014**, *47*, 1555-1562.
6. Nugent, P. S.; Rhodus, V. L.; Pham, T.; Forrest, K.; Wojtas, L.; Space, B.; Zaworotko, M. J. A Robust Molecular Porous Material with High CO2 Uptake and Selectivity. *J. Am. Chem. Soc.* **2013,** *135*, 10950-10953.
7. Chae, H. K.; Siberio-Pérez, D. Y.; Kim, J.; Go, Y.; Eddaoudi, M.; Matzger, A. J.; O'Keeffe, M.; Yaghi, O. M. A route to high surface area, porosity and inclusion of large molecules in crystals. *Nature* **2004**, *427*,523–527.
8. Schukraft, G. E. M.; Ayala, S., Jr.; Dick, B. L.; Cohen, S. M. Isoreticular Expansion of polyMOFs Achieves High Surface Area Materials. *Chem. Commun*. **2017**, *53*, 10684-10687.
9. Eddaoudi, M.; Kim, J.; Rosi, N.; Vodak, D.; Wachter, J.; O'Keeffe, M.; Yaghi, O. M., Systematic Design of Pore Size and Functionality in Isoreticular MOFs and Their Application in Methane Storage. *Science* **2002,** *295*, 469-472.
10. McKellar, S. C.; Sotelo, J.; Greenaway, A.; Mowat, J. P. S.; Kvam, O.; Morrison, C. A.; Wright, P. A.; Moggach, S. A., Pore shape modification of a microporous metal–organic framework using high pressure: accessing a new phase with oversized guest molecules. *Chem. Mater*. **2016,** *28*, 466-473.
11. Xue, D-X.; Belmabkhout,Y.; Shekhah, O.; Jiang, H.; Adil, K.; Cairns, A. J.; Eddaoudi, M. Tunable Rare Earth fcu-MOF Platform: Access to Adsorption Kinetics Driven Gas/Vapor Separations via Pore Size Contraction. *J. Am. Chem. Soc.* **2015**, *137*, 5034-5040.
12. Rieth, A. J.; Wright, A. M.; Rao, S.; Kim, H.; LaPotin, A. D.; Wang, E. N.; Dincă, M. *J. Am. Chem. Soc.* **2018**, *140*, 17591-17596.

13. Zhou, W.; Wu, H.; Yildirim, T., Enhanced H2 Adsorption in Isostructural Metal−Organic Frameworks with Open Metal Sites: Strong Dependence of the Binding Strength on Metal Ions. *J. Am. Chem. Soc*. **2008,** *130*, 15268-15269.
14. Kapelewski, M. T.; Geier, S. J.; Hudson, M. R.; Stück, D.; Mason, J. A.; Nelson, J. N.; Xiao, D. J.; Hulvey, Z.; Gilmour, E.; FitzGerald, S. A.; Head-Gordon, M.; Brown, C. M.; Long, J. R. M_2(m‑dobdc) (M = Mg, Mn, Fe, Co, Ni) Metal−Organic Frameworks Exhibiting Increased Charge Density and Enhanced H2 Binding at the Open Metal Sites. *J. Am. Chem. Soc*. **2014**, *136*, 12119−12129.
15. Wu, H.; Zhou, W.; Yildirim, T. High-Capacity Methane Storage in Metal-Organic Frameworks M2(dhtp): The Important Role of Open Metal Sites. *J. Am. Chem. Soc*. **2009**, *131*, 4995–5000.
16. Millward, A. R.; Yaghi, O. M., Metal−Organic Frameworks with Exceptionally High Capacity for Storage of Carbon Dioxide at Room Temperature. *J. Am. Chem. Soc*. **2005,** *127*, 17998-17999.
17. Cadiau, A.; Adil, K.; Bhatt, P. M.; Belmabkhout, Y.; Eddaoudi, M., A metal-organic framework-based splitter for separating propylene from propane. *Science* **2016,** *353*, 137-140.
18. Kato, S.; Saga, Y.; Kojima, M.; Fuse, H.; Matsunaga, S.; Fukatsu, A.; Kondo, M.; Masaoka, S.; Kanai, M. Hybrid Catalysis Enabling Room-Temperature Hydrogen Gas Release from N-Heterocycles and Tetrahydronaphthalenes. *J. Am. Chem. Soc*., **2017,** *139*, 2204-2207.
19. Seo, J. S.; Whang, D.; Lee, H.; Jun, S. I.; Oh, S.; Jeon, Y. J.; Kim, K. A homochiral metal-organic porous material for enantioselective separation and catalysis. *Nature* **2000**, *404*, 982-986.
20. Herm, Z. R.; Bloch, E. D.; Long, J. R. Hydrocarbon Separations in Metal−Organic Frameworks. *Chem. Mater*. **2014**, *26*, 323−338.
21. Sholl, D. S.; Lively, R. P. Seven chemical separations to change the world. *Nature* **2016**, *532*, 435–437.
22. Yang, Q.-Y.; Lama, P.; Sen, S.; Lusi, M.; Chen K.-J.; Gao W.-Y.; Shivanna, M.; Pham, T.; Hosono, N.; Kusaka, S.; Perry, J. J.; Ma, S.; Space, B.; Barbour L. J.; Kitagawa, S.; Zaworotko, M. J. Reversible Switching between Highly Porous and Nonporous Phases of an Interpenetrated Diamondoid Coordination Network That Exhibits Gate-Opening at Methane Storage Pressures. *Angew. Chem. Int. Ed*. **2018**, *57*, 5684-5689.
23. Kivi, C. E.; Gelfand, B. S.; Dureckova, H.; Ho, H. T. K.; Ma, C.; Shimizu, G. K. H.; Woo, T. K.; Song, D. 3D porous metal–organic framework for selective adsorption of methane over dinitrogen under ambient pressure. *Chem. Commun*., **2018**, *54*, 14104-14107.
24. Ma, L. Q.; Abney, C.; Lin, W. B. Enantioselective catalysis with homochiral metal-organic frameworks. *Chem .Soc. Rev*. **2009**, *38*, 1248-1256.
25. Lee, J.; Farha, O. K.; Roberts, J.; Scheidt, K. A.; Nguyen, S. T.; Hupp, J. T. Metal-organic framework materials as catalysts. *Chem. Soc. Rev*. **2009**, *38*, 1450-1459.
26. Palomba, J. M.; Credille, C. V.; Kalaj, M.; DeCoste, J. B.; Peterson, G. W.; Tovar, T. M.; Cohen, S. M. High-throughput screening of solid-state catalysts for nerve agent degradation. *Chem. Commun*., **2018**, *54*, 5768-5771.
27. Dinh, K. T.; Sullivan, M. M.; Serna, P.; Meyer, R. J.; Dincă, M.; Román-Leshkov, Y. A. Viewpoint on Partial Oxidation of Methane to Methanol Using Cu- and Fe-exchanged Zeolites. *ACS Catal*. **2018**, *8*, 8306-8313.
28. Campbell, M. G.; Dincă, M. Metal–Organic Frameworks as Active Materials in Electronic Sensor Devices. *Sensors* **2017**, *17*, 1108-1119.
29. Campbell, M. G.; Liu, S. F.; Swager, T. M.; Dincă, M. Chemiresistive Sensor Arrays from Conductive 2D Metal–Organic Frameworks. *J. Am. Chem. Soc.* **2015**, *137*, 13780-13783.

30. Gassensmith, J. J.; Kim, J. Y.; Holcroft, J. M.; Farha, O. K.; Stoddart, J. F.; Hupp, J. T.; Jeong, N. C. A Metal–Organic Framework-Based Material for Electrochemical Sensing of Carbon Dioxide. *J. Am. Chem. Soc.* **2014**, *136*, 8277-8282.
31. Wei, L.; Li, B.; Zhang, Q.; Chen, L.; Zeng, X. C., Monopolar Magnetic MOF-74 with Hybrid Node Ni–Fe. *J. Phys.Chem. C* **2016,** *120*, 26908-26914.
32. Xu, J.; Blaakmeer, E. S. M.; Lipton, A. S.; McDonald, T. M.; Liu, Y. M.; Smit, B.; Long, J. R.; Kentgens, A. P. M.; Reimer, J. A. Uncovering the Local Magnesium Environment in the Metal−Organic Framework Mg_2(dobpdc) Using ^{25}Mg NMR Spectroscopy. *J. Phys. Chem. C.* **2017**, *121*, 19938−19945.
33. Li, W.; Sun, L.; Qi, J.; Jarillo-Herrero, P.; Dincă, M.; Li, J. High Temperature Ferromagnetism in π-Conjugated Two-Dimensional Metal-Organic Frameworks. *Chem. Sci*. **2017**, *8*, 2859-2867.
34. Horcajada, P.; Serre, C.; Vallet-Regí, M.; Sebban, M.; Taulelle, F.; Férey, G. Metal-organic frameworks as efficient materials for drug delivery. *Angew. Chem. Inter. Ed*. **2006,** *45* , 5974-5978.
35. Orellana-Tavra, C.; Baxter, E. F.; Tian, T.; Bennett, T. D.; Slater, N. K. H.; Cheetham, A. K.; Fairen-Jimenez, D. Amorphous metal–organic frameworks for drug delivery. *Chem. Commun*., **2015**, *51*, 13878—13881.
36. Rieth, A. J.; Dincă, M. Controlled Gas Uptake in Metal-Organic Frameworks with Record Ammonia Sorption. *J. Am. Chem. Soc*. **2018**, *140*, 3461-3466.
37. Howarth, A. J.; Liu, Y.; Li, P.; Li, Z.; Wang, T. C.; Hupp, J. T.; Farha, O. K., Chemical, thermal and mechanical stabilities of metal–organic frameworks. *Nat. Rev. Mater*. **2016,** *1*, 15018-15034.
38. Denny, M. S., Jr., Kalaj, M.; Bentz, K. C.; Cohen, S. M. Multicomponent Metal–organic Framework Membranes for Advanced Functional Composites. *Chem. Sci*. **2018**, *9*, 8842-8849.
39. Yang, P.; Zhao, W.; Shkurenko, A.; Belmabkhout, Y.; Eddaoudi, M.; Dong, X.; Alshareef, H. N.; Khashab, N. M. Polyoxometalate–Cyclodextrin Metal–Organic Frameworks: From Tunable Structure to Customized Storage Functionality. J. Am. Chem. Soc. **2019**. DOI: 10.1021/jacs.8b11998
40. Bloch, W. M.; Burgun, A.; Coghlan, C. J.; Lee, R.; Coote, M. L.; Doonan, C. J.; Sumby, C. J. Capturing snapshots of post-synthetic metallation chemistry in metal-organic frameworks. *Nat Chem*. **2014**, *6*, 906-912.
41. You, W.; Liu, Y.; Howe, J. D.; Tang, D.; Sholl, D. S. Tuning Binding Tendencies of Small Molecules in Metal–Organic Frameworks with Open Metal Sites by Metal Substitution and Linker Functionalization. *J. Phys. Chem. C* **2018**, *122*, 27486-27494.
42. Demir, H.; Walton, K. S.; Sholl, D. S. Computational Screening of Functionalized UiO-66 Materials for Selective Contaminant Removal from Air. *J. Phys. Chem. C* **2017**, *121*, 20396-20406.
43. Tranchemontagne, D. J.; Hunt, J. R.; Yaghi, O. M., Room temperature synthesis of metal-organic frameworks: MOF-5, MOF-74, MOF-177, MOF-199, and IRMOF-0. *Tetrahedron* **2008,** *64*, 8553-8557.
44. Gygi, D.; Bloch, E. D.; Mason, J. A.; Hudson, M. R.; Gonzalez, M. I.; Siegelman, R. L.; Darwish, T. A.; Queen, W. L.; Brown, C. M.; Long, J. R. Hydrogen Storage in the Expanded Pore Metal−Organic Frameworks M_2(dobpdc) (M = Mg, Mn, Fe, Co, Ni, Zn). *Chem. Mater*. **2016**, *28*, 1128−1138.
45. Jiao, Y.; Morelock, C. R.; Burtch, N. C.; Mounfield, W. P., III.; Hungerford, J. T.; Walton, K. S. Tuning the Kinetic Water Stability and Adsorption Interactions of Mg-MOF-74 by Partial Substitution with Co or Ni. *Ind. Eng. Chem. Res.* **2015**, *54*, 12408-12414.
46. Schoedel, A.; Li, M.; Li D.; O'Keeffe, M.; Yaghi, O. M. Structures of Metal-Organic Frameworks with Rod Secondary Building Units. *Chem. Rev*. **2016**, *116*, 12466-12535.

47. Wang, L. J.; Deng, H.; Furukawa, H.; Gándara, F.; Cordova, K. E.; Peri, D.; Yaghi, O. M. Synthesis and characterization of metal-organic framework-74 containing 2, 4, 6, 8, and 10 different metals. *Inorg. Chem.* **2014,** *53*, 5881-5883.
48. Burrows, A. D. Mixed-component metal–organic frameworks (MC-MOFs): enhancing functionality through solid solution formation and surface modifications. *CrystEngComm* **2011,** *13*, 3623-3642.
49. Furukawa, H.; Müller, U.; Yaghi, O. M. "Heterogeneity within Order" in Metal–Organic Frameworks. *Angew. Chem. Inter. Ed*. **2015,** *54*, 3417-3430.
50. Sun, D.; Sun, F.; Deng, X.; Li, Z. Mixed-Metal Strategy on Metal−Organic Frameworks (MOFs) for Functionalities Expansion: Co Substitution Induces Aerobic Oxidation of Cyclohexene over Inactive Ni-MOF-74. *Inorg. Chem*. **2015**, *54*, 8639−8643.
51. Castillo-Blas, C.; de la Peña, V. A.; Puente-Orech, I.; de Paz, J. R.; Sáez-Puche, R.; Gutiérrez-Puebla, E.; Gándara, F.; Monge, Á. Addressed realization of multication complex arrangements in metal-organic frameworks. *Sci. Adv*. **2017**, *3*:e1700773.
52. Kim, D.; Coskun, Ali. Template-Directed Approach Towards the Realization of Ordered Heterogeneity in Bimetallic Metal–Organic Frameworks. *Angew. Chem. Int. Ed*. **2017**, *56*, 5071 –5076
53. James, S. L.; Adams, C. J.; Bolm, C.; Braga, D.; Collier, P.; Friscic, T.; Grepioni, F.; Harris, K. D. M.; Hyett, G.; Jones, W.; Krebs, A.; Mack, J.; Maini, L.; Orpen, A. G.; Parkin, I. P.; Shearouse, W. C.; Steed, J. W.; Waddell, D. C. Mechanochemistry: opportunities for new and cleaner synthesis. *Chem. Soc. Rev*. **2012,** *41*, 413-447.
54. Morris, W.; Doonan, C. J.; Furukawa, H.; Banerjee, R.; Yaghi, O. M.; Hupp, J. T. Crystals as Molecules: Postsynthesis Covalent Functionalization of Zeolitic Imidazolate Frameworks. *J. Am. Chem. Soc*. **2008,** *130*, 12626-12627.
55. Julien, P. A.; Užarević, K.; Katsenis, A. D.; Kimber, S. A. J.; Wang, T.; Farha, O. K.; Zhang, Y.; Casaban, J.; Germann, L. S.; Etter, M.; Dinnebier, R. E.; James, S. L.; Halasz, I.; Friščić, T. In Situ Monitoring and Mechanism of the Mechanochemical Formation of a Microporous MOF-74 Framework. *J. Am. Chem. Soc.* **2016,** *138*, 2929-2932.
56. Friščić, T. New opportunities for materials synthesis using mechanochemistry. *J. Mater. Chem*., **2010,** *20*, 7599-7605.
57. Friščić, T., Childs, S. L., Rizvi, S. A. A., Jones, W. The role of solvent in mechanochemical and sonochemical cocrystal formation: a solubility-based approach for predicting cocrystallisation outcome. *CrystEngComm* **2009**, *11*, 418-426.
58. Henkelis, S. E.; McCormick, L. J.; Cordes, D. B.; Slawin, A. M. Z.; Morris, R. E. Synthesis and crystallographic characterisation of $Mg(H_2dhta)(H_2O)_5{\cdot}H_2O$. *Inorg. Chem. Comm*., **2016**, *65*, 21-23.
59. Ghermani, N. E.; Morgant, G.; D'Angelo, J.; Desmaele, D.; Fraisse, B.; Bonhomme, F.; Dichi, E.; Sgahier, M. Covalently bonded infinite zigzag chain structure in a novel Zn(II) complex of 2,5-dihydroxy-1,6-benzenedicarboxylic acid. *Polyhedron* **2007**, *26*, 2880-2884.

Supporting Information

Mechanochemistry enables targeted synthesis of mixed-metal microporous metal-organic frameworks using pre-assembled precursors

Ghada Ayoub, Bahar Karadeniz, Ashlee J. Howarth, Omar K. Farha, Ivica Đilović, Luzia S. Germann, Robert E. Dinnebier, Krunoslav Užarević* Tomislav Friščić*

Table of Contents

S.1 Material and Methods

2,5-dihydroxyterephthalic acid (H_4**dhta**) was purchased from TCI America (Portland, OR, USA), ZnO, MgO, $Co(CH_3COO)_2 \cdot 4H_2O$, and $Cu(OH)_2$ were purchased from Sigma Aldrich (St. Louis, MO, USA). Methanol and dimethylformamide (DMF) were purchased from ACP Chemicals (Montreal, QC, CA). All chemicals were used without further purification.

FTIR-ATR spectroscopy. Fourier-transform infrared attenuated total reflectance (FTIR-ATR) were recorded on Bruker Vertex 70 spectrometer (Milton, ON, CA) with RockSolidT^M interferometer in the range of 4400-400 cm^{-1} , with 4 cm^{-1} step. FTIR spectra were analysed using Bruker OPUS software.

TGA and DSC experiments. Thermograms were collected using a TA Instruments TGA Q500 thermogravimetric analyser at a heating rate of 10°C/min from 25°C to 700°C under dynamic atmosphere of nitrogen and air. The flow rates of the purge gas and sample gas were set at 50 mL/min and 50 mL/min respectively. TGA curves were analyzed with TA Universal Analysis software.

Single crystal X-ray diffraction. Single crystals of $C_8H_{16}NiO_{12}$ were grown from water. A suitable crystal was selected and mounted on a diffractometer. Diffracted intensities were collected on Oxford Diffraction Ruby Nova diffractometer using CuKα radiation (λ=1.54184 Å) using ω-scans at 293(2) K. Data were prepared using the CrysAlis[1] program. A summary of general and crystal data, intensity data collection and final refinement parameters are presented in Table S1. The structures were solved by direct methods using SHELXS programme.[2] The refinement procedure by full-matrix least squares methods based on F^2 values against all reflections included anisotropic displacement parameters for all non-H atoms. All refinements were performed using SHELXL-97.[2] The SHELX programs operated within the WinGX[3] suite. Geometrical calculations and molecular graphics were done with PLATON[4] and MERCURY[5]. Supplementary crystallographic data set for the structure **3** is available through the Cambridge Structural Data base with deposition number 1893479. Copy of this information may be obtained free of charge from the director, CCDC, 12 Union Road, Cambridge, CB2 1EZ, UK (fax: +44 1223 336 033; e-mail: deposit@ccdc.cam.ac.uk or visit http://www.ccdc.cam.ac.uk).

Powder X-ray diffraction (PXRD). Powder X-ray diffraction (PXRD) patterns for phase analysis were collected using a Bruker D2 powder diffractometer equipped with a Cu*Kα* (λ=1.54060 Å) source and Lynxeye detector (Bruker AXS, Madison, WI) with a lower and upper discriminant of 0.110 V and 0.250 V respectively. The patterns were collected in the range of 5 ° to 40 ° 2θ.
PXRD pattern for crystal structure determination of Co-intermediate was collected using a Stoe Transmission Powder Diffraction System (STADI-P) equipped with a Ge(111) Johann-type monochromator from STOE & CIE with Mo$K\alpha_1$ radiation that was equipped with a linear position-sensitive MYTHEN 1K detector from Dectris Ltd. The pattern was collected in the range of 2 to 50 ° 2θ within 9 hours.
Phase analysis of PXRD patterns was conducted using Panalytical X'Pert Highscore Plus software. Experimental patterns (1, 2, 3) were compared to simulated patterns calculated from single crystal structures using Mercury software package. Crystal structure determination of $[Co(H_2O)_4(H_2$**dhta**$)\cdot 2H_2O]_n$ (**4**) was performed using TOPAS V5, see section S.11.[6]
Crystal structure determination of $[Co(H_2O)_4(H_2$**dhta**$)\cdot 2H_2O]_n$ (**4**) was performed by a Rietveld refinement, using the isostructural nickel compound **(3)** as starting model.[7] The peak profile was described using the

fundamental parameter approach as implemented in TOPAS during the refinement.[8] The background was modeled by Chebychev polynomials (13th order). The microstructure of **4** was modeled with a Lorentzian and Gaussian microstrain, and a Gaussian crystallite size parameter. During the final Rietveld refinement all lattice parameters, microstructural parameters, and cobalt ion were freely refined. The positions of water and the H_2**dhta** ligands were fixed, therefore, the comparison of Ni-O and Co-O bond lengths has to be handled with some caution. Cobalt acetate hydrate (CSD refcode FULWOY) was found and refined as side phase (ca. 6 w% abundance). Supplementary crystallographic data set for the structure is available through the Cambridge Structural Data base with deposition number 1894933. Copy of this information may be obtained free of charge from the director, CCDC, 12 Union Road, Cambridge, CB2 1EZ, UK (fax: +44 1223 336 033; e-mail: deposit@ccdc.cam.ac.uk or http://www.ccdc.cam.ac.uk).

SEM analysis

Scanning electron microscopy (SEM) images were recorded on a Hitachi SU8030 SEM. Prior to analysis, samples were coated with 4 nm of platinum.

N_2 isotherms

Nitrogen adsorption/desorption isotherms were recorded for each activated MOF sample using a Micromeritics TriStar (III) surface area analyzer at 77 K with the temperature held constant using liquid N_2 bath. Prior to analysis, approximately 100 mg of each MOF was activated overnight at 150 °C under a flow of dry nitrogen. BET modeling was performed to obtain the specific surface area ($m^2\ g^{-1}$).

S.2 Synthetic procedures

S.2.1 Mechanochemical synthesis of ZnCo-MOF-74 using water and MeOH as a liquid additive

All syntheses were performed (unless stated otherwise) in PMMA 10 mL jar, using one 4.0 g stainless steel ball and Retsch MM400 mixer mill operating at 30 Hz. 110 mg of H_4**dhta** (0.55 mmol) and 45.19 mg (0.55 mmol) of ZnO were placed in separate milling vessels with one 4.0 g stainless steel ball. Then 100 μL of H_2O was added and the reaction mixture and milling was done for 10 minutes to form the white and wet crystalline Zn intermediate of the formula $[Zn(H_2O)_2(H_2$**dhta**$)]_n$. To the latter intermediate, 66.03 mg of $CoCO_3$ was added along with 120 μL of MeOH and the reaction mixture was milled for 60 minutes to form a brown crystalline ZnCo-MOF-74 product. The product was washed twice with DMF then filtered, dried, and evacuated at 100 ˚C. The color of the end-product is light brown. PXRD measurements was performed immediately after the 60 min and the reaction is considered to be complete when the ZnO reflections are not visible in the PXRD pattern.

S.2.2 Mechanochemical synthesis of ZnMg-MOF-74 using water and MeOH as a grinding liquid

110 mg of H_4**dhta** (0.55 mmol) and 45.19 mg of ZnO (0.55 mmol) were placed in separate milling vessels with one 4.0 g stainless steel ball. Then 100 μL of water was added, and the reaction mixture milled for 10 minutes. To the latter Zn intermediate 22.37 mg of MgO was added to the milling vessel with 120 μL of MeOH to form a pale yellow crystalline ZnMg-MOF-74 product. The sample was washed twice with DMF then filtered, dried, and evacuated at 100 ˚C.

S.2.3 Mechanochemical synthesis of ZnCu-MOF-74 using MeOH as the grinding liquid

110 mg of H_4**dhta** (0.55 mmol) and 45.19 mg (0.55 mmol) of ZnO were placed in separate milling vessels with one 4.0 g stainless steel ball. Then 100 μL of H_2O was added and the reaction mixture was milled for 10 minutes to form the white crystalline Zn intermediate having the formula $[Zn(H_2O)_2(H_2$**dhta**$)]_n$. To the

latter intermediate, 54.17 mg of $Cu(OH)_2$ (0.55 mmol) was added with 120 μL of MeOH as a liquid additive and the reaction mixture was milled for 60 minutes to form a dark-brown crystalline ZnCu-MOF-74 material. The product was washed twice with DMF then filtered, dried, and evacuated at 100 ˚C.

S.2.4 Mechanochemical synthesis of Mg-MOF-74 using MeOH as a grinding liquid

110 mg of H_4**dhta** (0.55 mmol) and 44.74 mg of MgO (0.55 mmol) were placed in separate milling vessels with one 4.0 g stainless steel ball. Then 250 μL of MeOH was added to one of milling vessels and the reaction mixture was milled for 105 minutes to form a pale-yellow crystalline product Mg MOF-74 material. Sample was then washed twice with DMF, filtered, then evacuated at 100 ˚C overnight.

S.2.5 Mechanochemical synthesis of MgZn-MOF-74 using MeOH as a grinding liquid

110 mg of H_4**dhta** (0.55 mmol) and 22.37 mg of MgO (0.55 mmol) were placed in separate milling vessels with one 4.0 g stainless steel ball. Then 100 μL of MeOH was added and milling was done for 10 minutes. To the latter monomeric complex, 45.19 mg of ZnO was added to the milling vessel with 120 μL of MeOH to form a pale yellow crystalline MgZn-MOF-74 product. The latter was washed twice with filtered, then evacuated at 100 ˚C overnight.

S.2.6 Mechanochemical synthesis of MgCo-MOF-74 using MeOH as a grinding liquid

110 mg of (H_4**dhta**) (0.55 mmol) and 22.37 mg of MgO (0.55 mmol) were placed in separate milling vessels with one 4.0 g stainless steel ball. Then 120 μL of MeOH was added and milling was done for 10 minutes. To the latter monomeric complex, 138.29 mg of $Co(OAc)_2.4H_2O$ (0.55mmol) (Ac: acetate) was added to the milling vessel with 120 μL of MeOH to form a light-brown crystalline MgCo-MOF-74 product. The latter was washed twice with DMF, filtered, then evacuated at 100 ˚C overnight

S.2.7 Mechanochemical synthesis of MgCa-MOF-74 using MeOH as a grinding liquid

110 mg of (H_4**dhta**) (0.55 mmol) and 22.37 mg of MgO (0.55 mmol) were placed in separate teflon-type milling vessels with one 4.0 g stainless steel ball. Then 50 μL of H_2O was added, and milling was done for 10 minutes. To the latter monomeric complex, 31 mg of CaO (0.55 mmol) was added to the milling vessel with 120 μL of MeOH and milling was performed for 90 minutes to form a pale yellow crystalline MgCa-MOF-74 product. The latter was washed with MeOH followed by washing with DMF, then evacuated at 100 ^{0}C overnight. MgO and CaO were calcined at 800 ^{0}C to remove any traces of water molecules.

S.2.8 Mechanochemical synthesis of NiZn-MOF-74 using MeOH as the grinding liquid

110 mg of H_4**dhta** (0.55 mmol) and 138.153 mg (0.55 mmol) of $Ni(OAc)_2.4H_2O$ were added to separate milling jars with one 4.0 g stainless steel ball. Then 80 μL of H_2O was added to one of the milling vessels and milling was done for 45 minutes to form a wet and green crystalline Ni intermediate. To the latter intermediate, 45.19 mg (0.55 mmol) of ZnO was added to the reaction mixture with 120 μL of MeOH and milling was continued for 60 minutes to form a light green crystalline material of NiZn-MOF-74. The product was washed twice with DMF then filtered, evacuated at 100 ˚C.

S.2.9 Mechanochemical synthesis of NiMg-MOF-74 using MeOH as the grinding liquid

110 mg of H_4**dhta** (0.55 mmol) and 138.153 mg (0.55 mmol) of $Ni(OAc)_2.4H_2O$ were added to separate milling jars with one 4.0 g stainless steel ball. Then 80 μL of H_2O was added to one of the milling vessels and milling was done for 45 minutes to form a wet and green crystalline Ni intermediate. To the latter intermediate, 22.37 mg (0.55 mmol) of MgO was added to the reaction mixture with 120 μL of MeOH and

milling was continued for 60 minutes to form a light green crystalline material of NiMg-MOF-74. The product was washed twice with DMF then filtered, evacuated at 100 ˚C.

S.2.10 Mechanochemical synthesis of NiCo-MOF-74 using MeOH as the grinding liquid

110 mg of H_4**dhta** (0.55 mmol) and 138.153 mg (0.55 mmol) of $Ni(OAc)_2.4H_2O$ were added to separate milling jars with one 4.0 g stainless steel ball. Then 80 μL of H_2O was added to one of the milling vessels and milling was done for 45 minutes to form a wet and green crystalline Ni intermediate $[Ni(H_2\textbf{dhta})(H_2O)_4{\cdot}2H_2O]_n$.. To the latter intermediate, 138.286 mg (0.55 mmol) of $Co(OAc)_2.4H_2O$ was added to the reaction mixture with 120 μL of MeOH and milling was continued for 60 minutes to form a light brown crystalline material of NiCo-MOF-74. The product was washed twice with DMF then filtered, evacuated at 100 ˚C.

S.2.11 Mechanochemical synthesis of Co-MOF-74 using MeOH as the grinding liquid

The mass of the reactants used was 110 mg of H_4**dhta** (0.55 mmol) and 276.58 mg of $Co(OAc)_2.4H_2O$ (1.11 mmol). Reactants were added to the milling vessel, followed by the addition of 200 μL of DMF then the milling was performed for 90 min. The color of the end product is light brown. PXRD measurements was done immediately after the 90 min.

S.2.12 Mechanochemical synthesis of CoZn-MOF-74 using MeOH as the grinding liquid

110 mg of H_4**dhta** (0.55 mmol) and 138.286 mg (0.55 mmol) of $Co(OAc)_2.4H_2O$ were added to separate milling jars with one 4 g stainless steel ball. Then 80 μL of H_2O was added to one of the milling vessels and milling was done for 45 minutes to form a pink crystalline Co intermediate $[Co(H_2\textbf{dhta})(H_2O)_4{\cdot}2H_2O]_n$. To the latter intermediate, 45.19 mg (0.55 mmol) of ZnO was added to the reaction mixture with 120 μL of MeOH and milling was continued for 60 minutes to form a light brown crystalline material of CoZn-MOF-74. The product was washed twice with DMF then filtered, evacuated at 100 ˚C.

S.2.13 Mechanochemical synthesis of CoMg-MOF-74 using MeOH as the grinding liquid

110 mg of H_4**dhta** (0.55 mmol) and 138.286 mg (0.55 mmol) of $Co(OAc)_2.4H_2O$ were added to separate milling jars with one 4.0 g stainless steel ball. Then 80 μL of H_2O was added to one of the milling vessels and milling was done for 45 minutes to form a pink crystalline Co intermediate $[Co(H_2\textbf{dhta})(H_2O)_4{\cdot}2H_2O]_n$. To the latter intermediate, 22.37 mg (0.55 mmol) of MgO was added to the reaction mixture with 120 μL of MeOH and milling was continued for 60 minutes to form a light brown crystalline material of CoMg-MOF-74. The product was washed twice with DMF then filtered, evacuated at 100 ˚C.

S.2.14 Mechanochemical synthesis of CoCu-MOF-74 using MeOH as the grinding liquid

110 mg of H_4**dhta** (0.55 mmol) and 138.286 mg (0.55 mmol) of $Co(OAc)_2.4H_2O$ were added to separate milling jars with one 4.0 g stainless steel ball. Then 80 μL of H_2O was added to one of the milling vessels and milling was done for 45 minutes to form a pink crystalline Co intermediate $[Co(\textbf{dhta})(H_2O)_4{\cdot}2H_2O]_n$. To the latter intermediate, 54.16 mg (0.55 mmol) of $Cu(OH)_2$ was added to the reaction mixture with 120 μL of MeOH and milling was continued for 60 minutes to form a light brown crystalline material of CoCu-MOF-74. The product was washed twice with DMF then filtered, evacuated at 100 ˚C.

S.3 Activation of the MM-MOF-74 materials prior to characterization

The MM-MOF-74 samples (~100 mg) were washed using a Soxhlet extraction method that utilizes hot methanol for 24 hours. This was done to get rid of any excess linkers that were present in the sample and that are difficult to remove by washing with methanol at room temperature. After washing, the samples were transferred into sorption tubes and outgassed on a SmartVacPrep (Micromeritics, Norcross, GA, USA) and heated slowly to 150 ^{0}C for a period of five hours. Heating slowly was crucial for activation because the slower the solvent is removed, the less strain is applied to the framework, and consequently structural damage is less likely. After this activation step, nitrogen adsorption/desorption isotherms were recorded using a micromeritics tristar surface area analyzer at 77 K from which the surface area (m^2/g) was calculated.

S.4. Digestion of the MM'-MOF-74 samples for ICP analysis

All the measurements for the metal detection of Zn, Cu, Co, Ni, Mg, and Ca was done on ICP-MS (Thermo iCAPQ c). All solid samples (0.5-1 mg) were first digested using 200 microliters of concentrated hydrogen peroxide purchased from Aldrich Chemical Co., followed by adding concentrated nitric acid and hydrochloric acid in 1:3 ratio. The solid MOF samples were dissolved completely upon this treatment. Samples were diluted with deionized water to a total volume of 100 mL in a volumetric flask. Then 50 μL of the latter solution was diluted with (DI) to a total volume of 100 mL in a volumetric flask. The solutions were then transferred to low density polyethylene tubes purchased from Fisher Scientific International Inc. All glassware for ICP-OES was rinsed thoroughly for a minimum of five times with DI water. Standards were prepared from Inorganic Ventures' multi-element standard solutions of Mg, Ca, Co, Ni, Zn, and Cu.

S.5 Characterization of ZnMg-, ZnCo-, and ZnCu-MOF-74 materials

S.5.1 FTIR-ATR spectra for ZnM'-MOF-74 materials

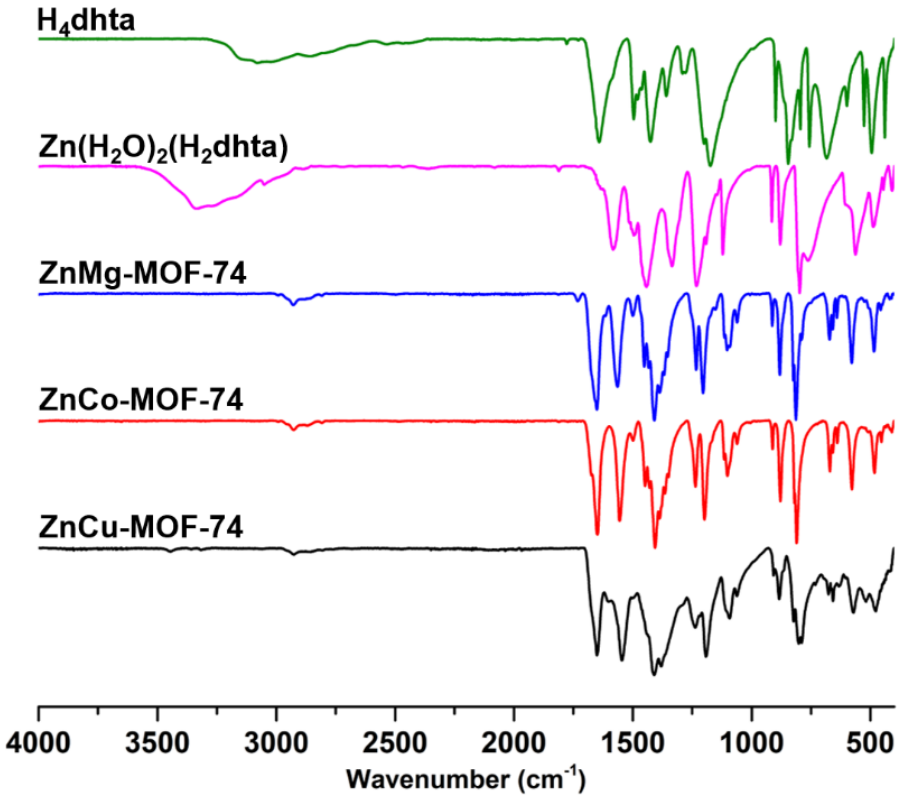

Figure S1. Comparison of FTIR-ATR spectra for (top-to-bottom): H_4**dhta** (green curve), $[Zn(H_2O)_2(H_2$**dhta**$)]_n$ (pink curve), ZnMg-MOF-74 (blue curve), ZnCo-MOF-74 (red curve), and ZnCu-MOF-74 (black curve) materials. The FTIR-ATR spectra of the ZnMg-, ZnCo-, and ZnCu-MOF-74 materials closely resembles each other. No trace of starting H_4**dhta** was observed in the as-synthesized products.

S.5.2 SEM images of ZnM'-MOF-74 materials

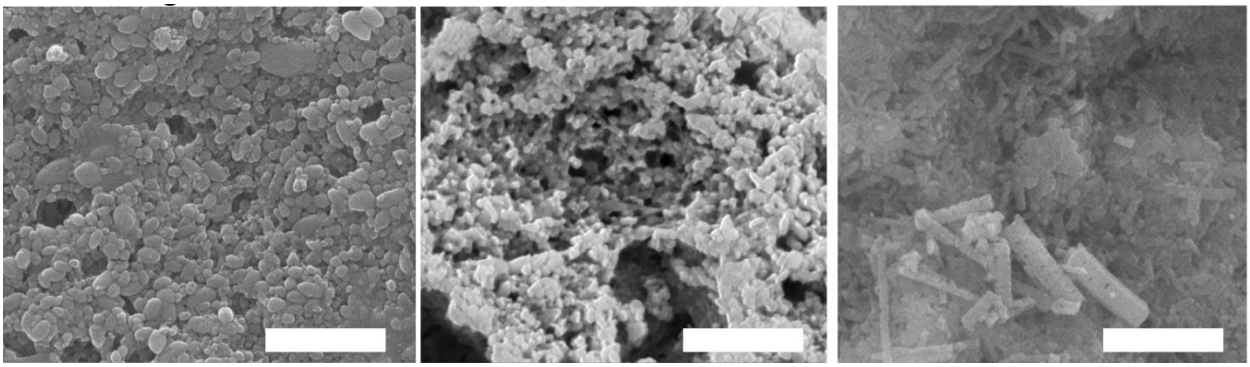

Figure S2. SEM image of ZnMg- (left side), ZnCo- (middle), and ZnCu-MOF-74 (right side) materials. Scale bar corresponds to 1 μm.

S.5.3 TGA analysis of ZnM'-MOF-74 materials

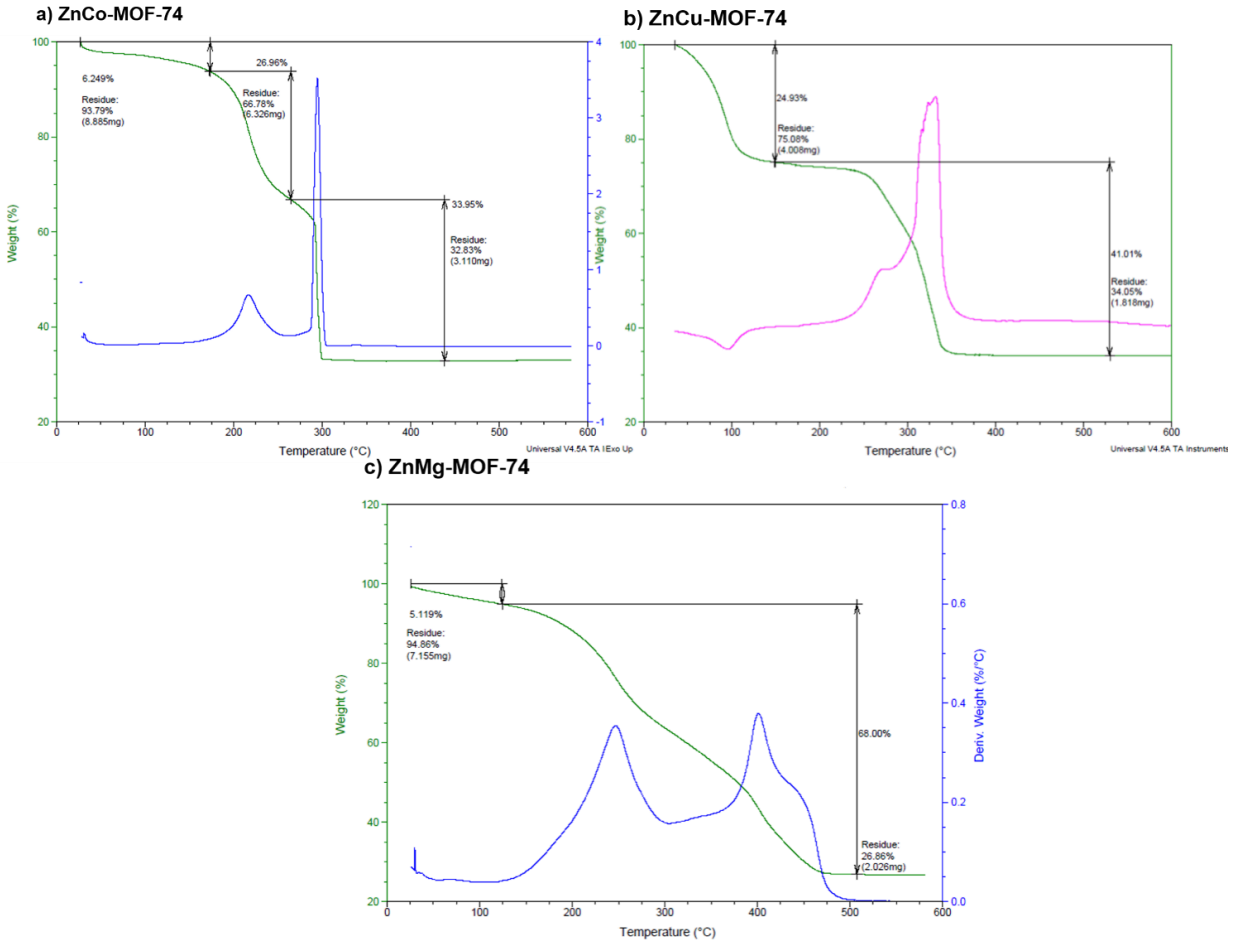

Figure S3. The TGA thermogram (recorded in air, 30-700 °C, heating rate 10 °C/min) of a) ZnCo-MOF-74, b) ZnCu-MOF-74, and c) ZnMg-MOF-74. In all cases, the first degradation step most likely corresponds to loss of included solvent molecules, the second step corresponds to the ligand decomposition and therefore MOF structural damage, and the final decomposition leads to formation of ZnO, MgO, CuO.

S.6 Characterization of MgZn- and MgCo-MOF-74 materials

S.6.1 FTIR-ATR spectra of MgM'-MOF-74 materials

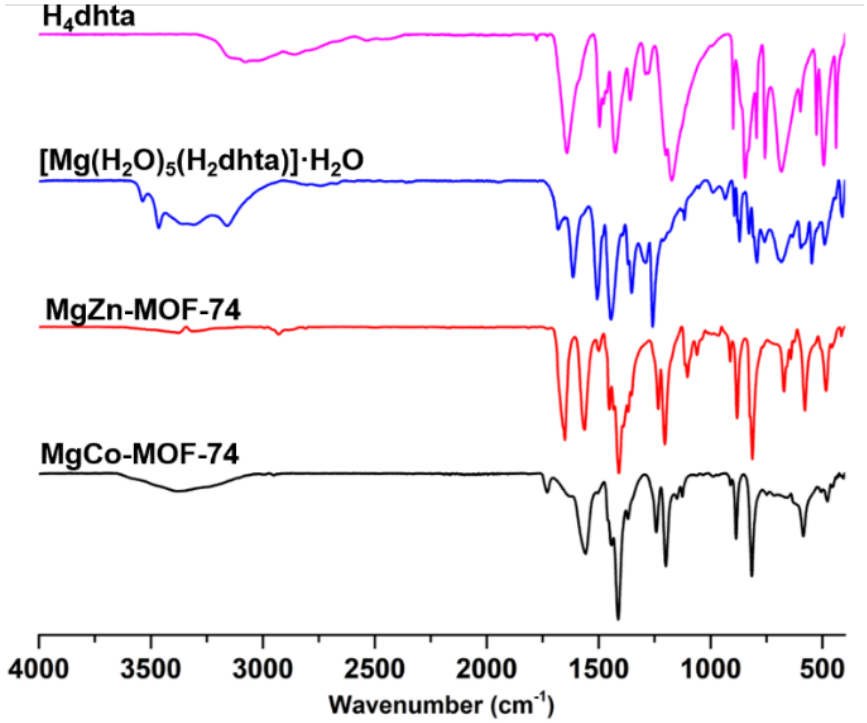

Figure S4. Comparison of FTIR-ATR spectra for (top-to-bottom): H_4**dhta** (pink curve), $[Mg(H_2O)_5(H_2$**dhta**$)].H_2O$ (blue curve) , MgZn-MOF-74 (red curve) and MgCo-MOF-74 (black curve) materials. The FTIR-ATR spectrum of the MgZn- and MgCo -MOF-74 materials closely resembles each other. No traces of starting H_4**dhta** is observable in the as-synthesized products.

S.6.2 SEM images of MgM'-MOF-74 materials

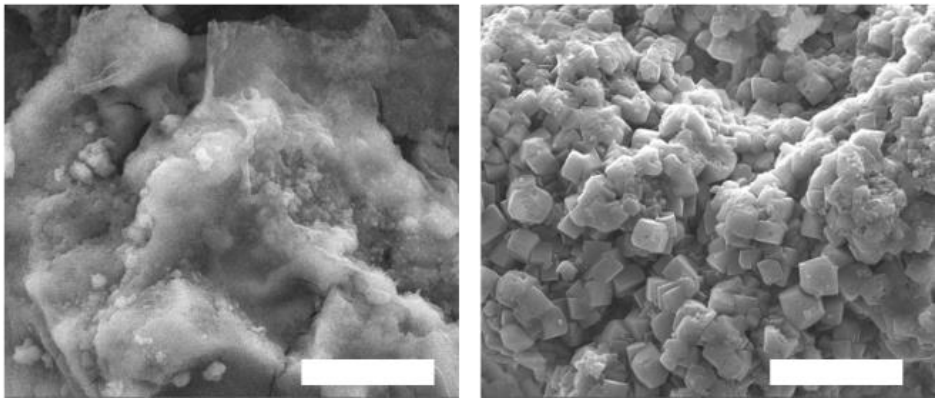

Figure S5. SEM image of MgZn-MOF-74 (left) and MgCo-MOF-74 (right) material. Scale bar corresponds to 5 μm magnification.

S.6.3 TGA analysis of MgM'-MOF-74 materials

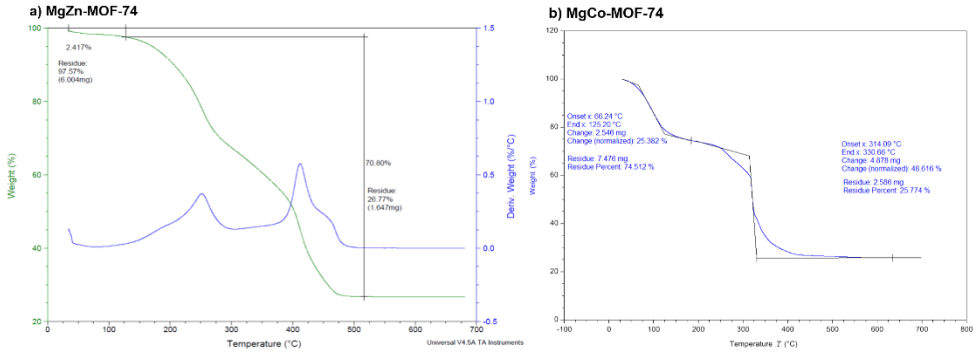

Figure S6. The TGA thermogram (recorded in air, 30-700 °C, heating rate 10 °C/min) of a) MgZn-MOF-74 and b) MgCo-MOF-74. In all cases, the first degradation step most likely corresponds to loss of included solvent molecules, the second step corresponds to the ligand decomposition and therefore MOF structural damage, and the final decomposition leads to formation of ZnO, MgO, and Co_3O_4.

S.7 Characterization of MgCa-MOF-74 material

S.7.1 FTIR-ATR spectra for the MgCa-MOF-74 material

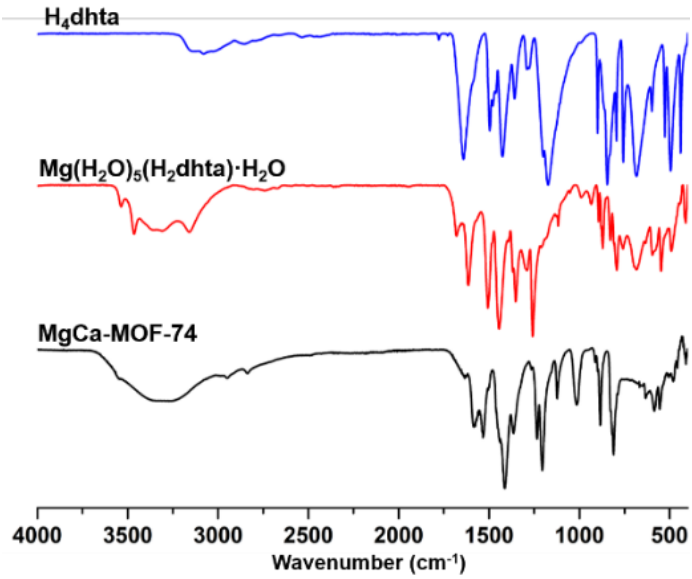

Figure S7. Comparison of FTIR-ATR spectra for (top-to-bottom): H_4**dhta** (blue curve), $Mg(H_2O)_5(H_2$**dhta**$)\cdot H_2O$ (red curve), and MgCa-MOF-74 (black curve) materials.

S.7.2 SEM imaging of MgCa-MOF-74 material.

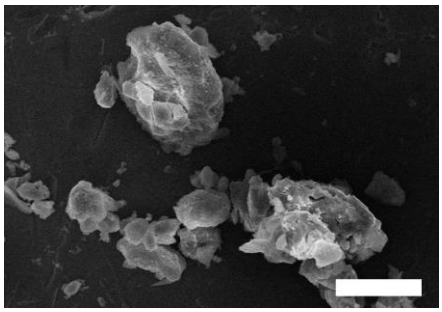

Figure S8. SEM image of MgCa-MOF-74 material. Scale bar corresponds to 20 µm magnification.

S.7.3 TGA analysis MgCa-MOF-74 material

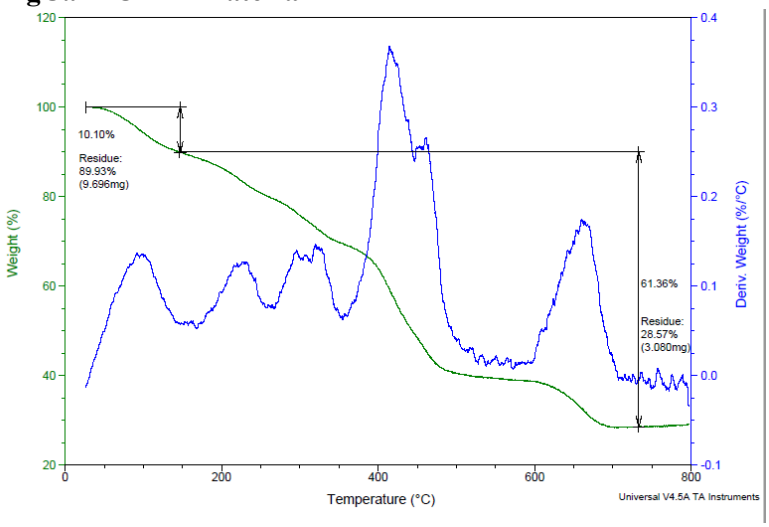

Figure S9. Thermogram (recorded in air, 30-800 °C, heating rate 10 °C/min) for heating of MgCa-MOF-74. The first step in TGA corresponds to egress of included solvent from the MOF material. The rest of the thermogram corresponds to the to the decomposition of MOF-74 material including the organic ligand. The final product of thermal decomposition is ZnO and CaO.

S.7.4 Isotherm plot and pore size distribution of MgCa-MOF-74

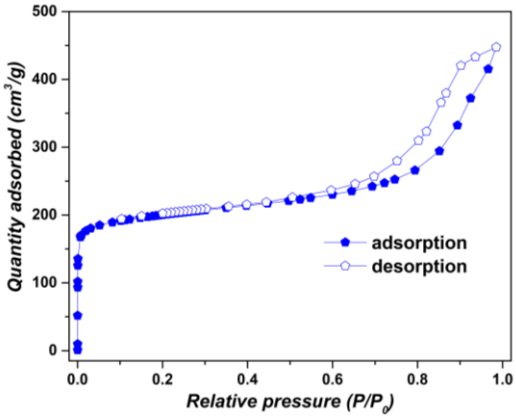

Figure S10. Isotherm plot of MgCa-MOF-74 material recorded at 77 K.

S.8 Characterization of NiZn-, NiMg and NiCo-MOF-74 materials

S.8.1 FTIR-ATR spectra for NiM'-MOF-74 materials

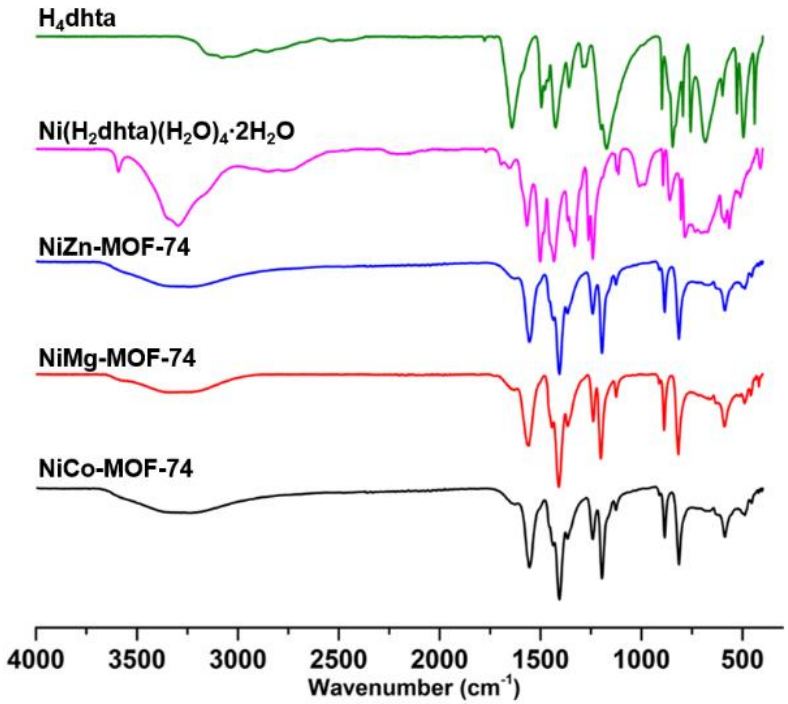

Figure S11. Comparison of FTIR-ATR spectra for (top-to-bottom): H_4**dhta** (green curve), Ni intermediate (pink curve), NiZn- (blue curve), NiMg- (red curve), and NiCo-MOF-74 (black curve) materials. The FTIR-ATR spectrum of the NiZn-, NiMg-, and NiCo-MOF-74 materials closely resembles each other. No trace of starting H_4**dhta** is observable in the as-synthesized products.

S.8.2 SEM images for NiM'-MOF-74 materials

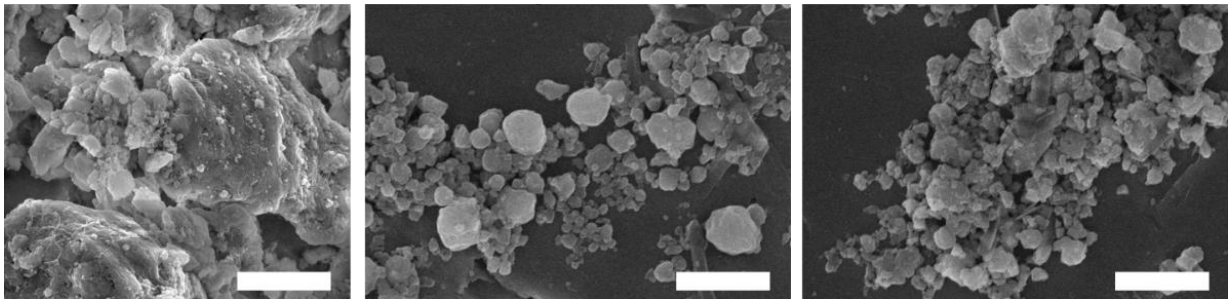

Figure S12. SEM images of (from left to right) NiZn- (left), NiMg- (middle), NiCo-MOF-74 (right) materials. Scale bar corresponds to 10, 5, and 5 μm magnification, respectively.

S.8.3 TGA analysis for NiM'-MOF-74 materials

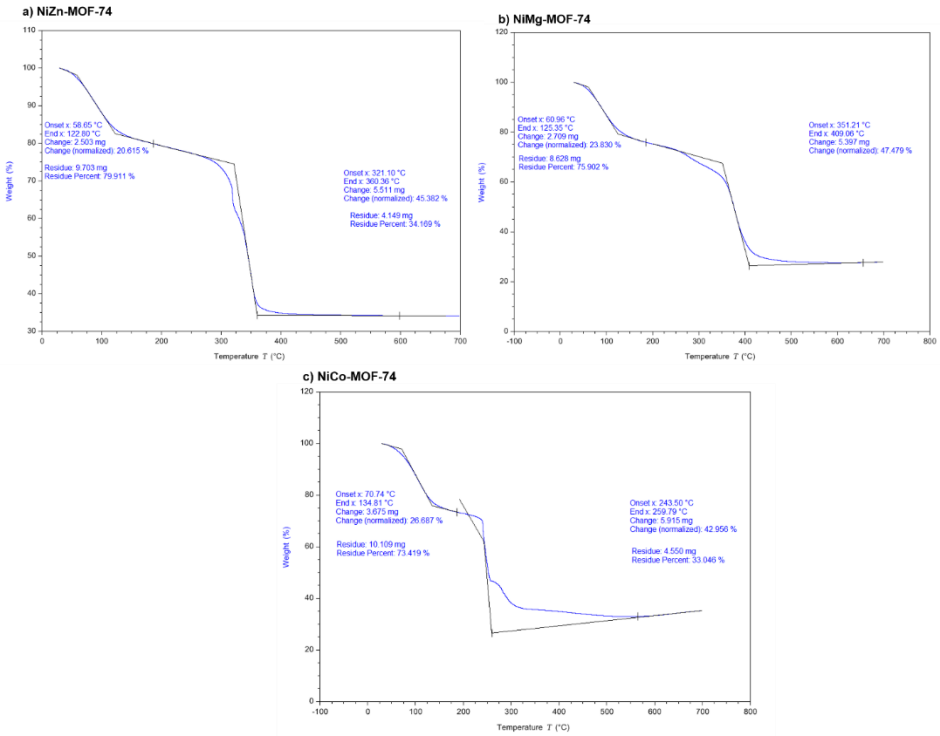

Figure S13. The TGA thermogram (recorded in air, 30-700 °C, heating rate 10 °C/min) of a) NiZn-MOF-74, (b) NiMg-MOF-74, and (c) NiCo-MOF-74. In all cases, the first degradation step most likely corresponds to loss of included solvent molecules, the second step corresponds to the MOF-74 decomposition and the ligand decomposition, and the final decomposition leads to formation of the metal oxides (NiO, ZnO, MgO, Co_3O_4).

S.8.4 Nitrogen isotherm plot for NiZn-MOF-74

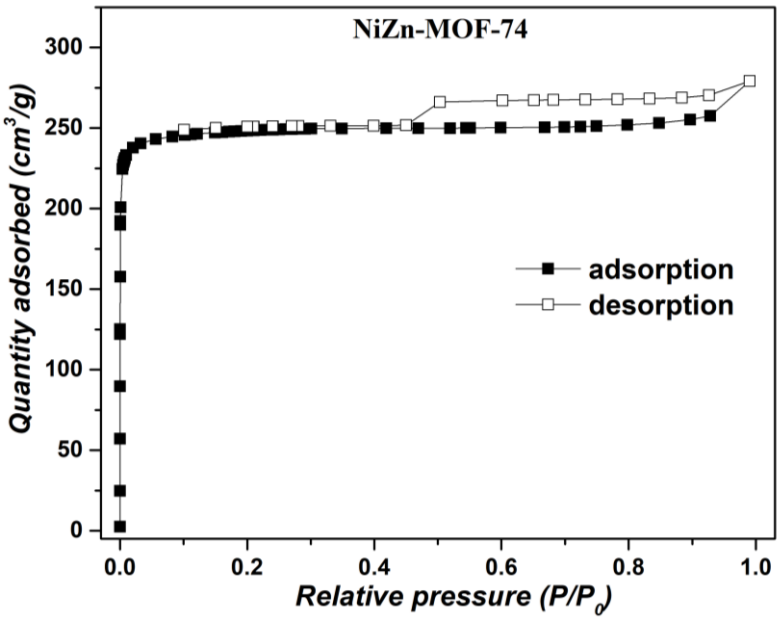

Figure S14. Nitrogen adsorption and desorption isotherms of NiZn-MOF-74 material.

S.8.5 Nitrogen isotherm plots for NiMg-MOF-74

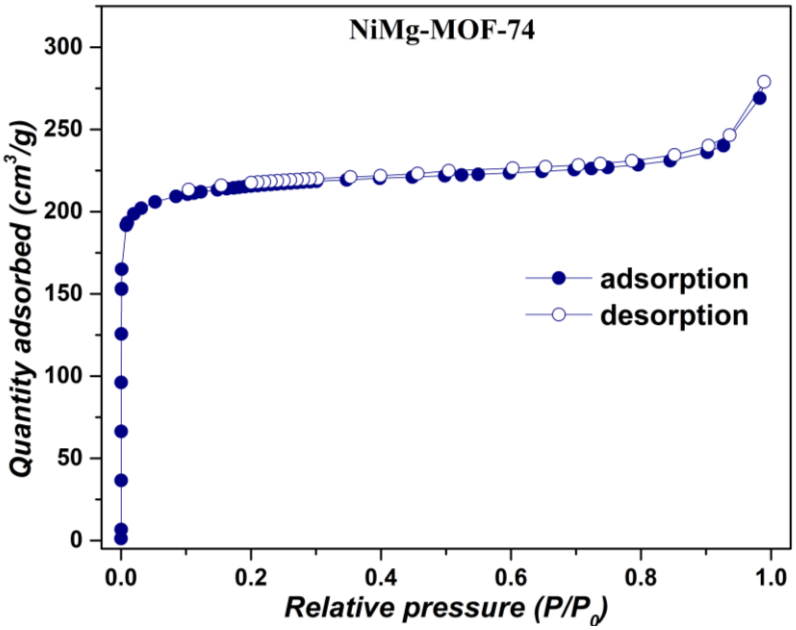

Figure S15. Nitrogen adsorption and desorption isotherms of NiMg-MOF-74 material.

S.8.6 Nitrogen isotherm plots of NiCo-MOF-74

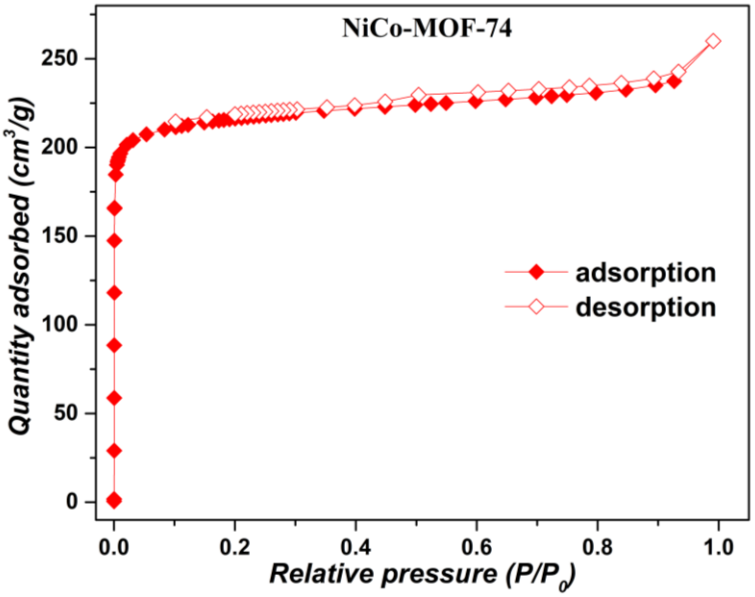

Figure S16. Nitrogen adsorption and desorption isotherms of NiCo-MOF-74.

S.9 Characterization of CoZn-, CoMg-, and CoCu-MOF-74 materials

S.9.1 FTIR-ATR spectra of CoM'-MOF-74 materials

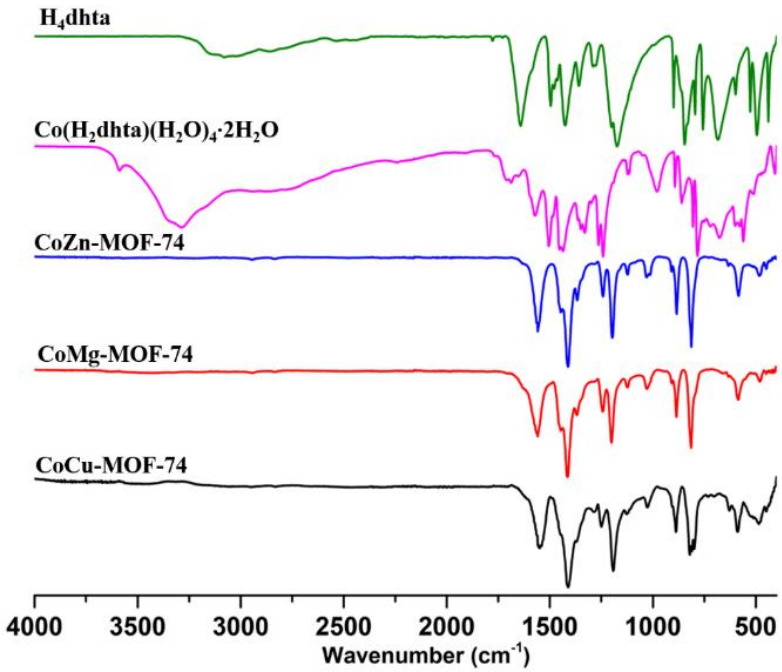

Figure S17. Comparison of FTIR-ATR spectra for (top-to-bottom): H_4**dhta** (green curve), Co intermediate $[Co(H_2$**dhta**$)(H_2O)_4 \cdot 2H_2O]_n$ (pink curve) , CoZn- (blue curve), CoMg- (red curve), and CoCu-MOF-74 (black curve) materials. The FTIR-ATR spectrum of the CoZn-, CoMg-, and CoCu-MOF-74 materials closely resembles each other. No trace of starting H_4**dhta** is observable in the as-synthesized products.

S.9.2 SEM images for CoM'-MOF-74 materials

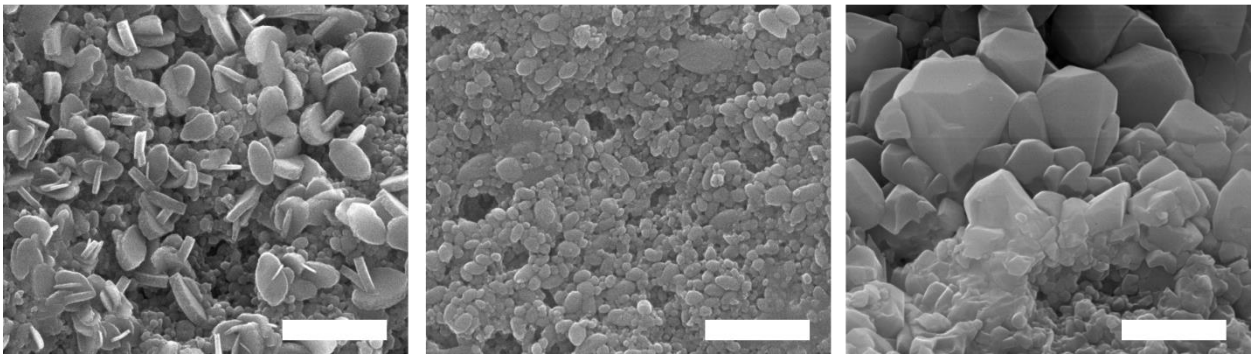

Figure S18. SEM images of CoZn- (left), CoMg- (middle), and CoCu-MOF-74 (right) materials. Scale bar corresponds to at 1 μm magnification.

S.9.3 TGA analysis of CoM'-MOF-74 materials

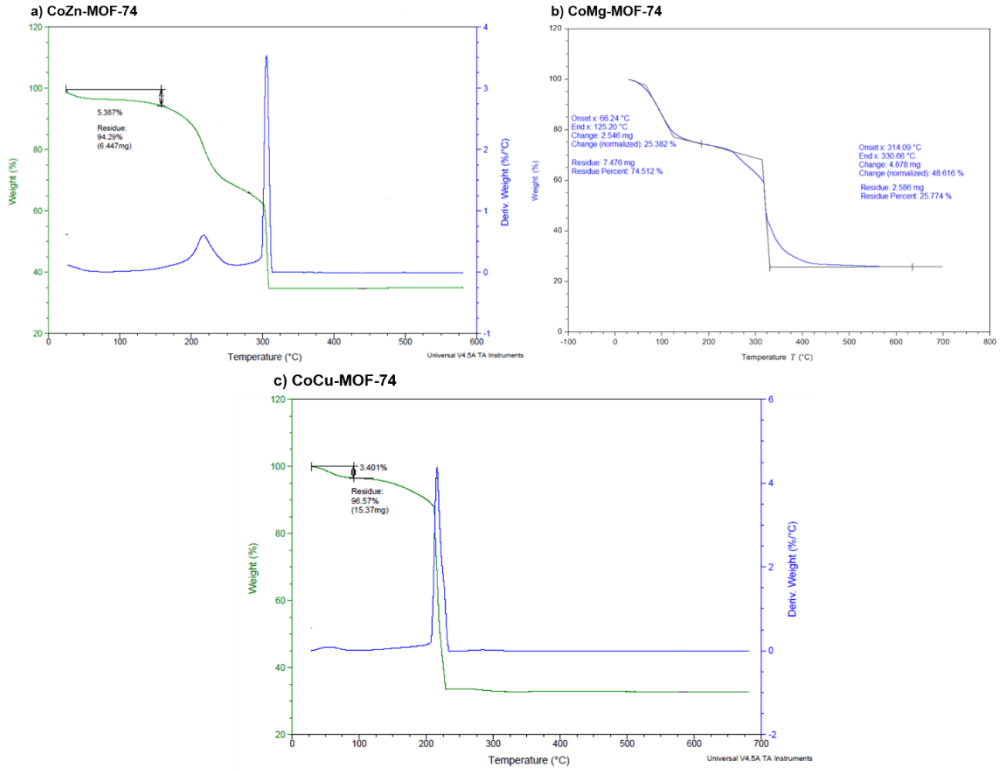

Figure S19. The TGA thermogram (recorded in air, 30-700 °C, heating rate 10 °C/min) of a) CoZn-MOF-74, CoMg-MOF-74, and c) CoCu-MOF-74. In all cases, the first degradation step most likely corresponds to loss of included solvent molecules, the second step corresponds to the MOF-74 decomposition and the ligand decomposition, and the final decomposition leads to formation of the metal oxides (ZnO, MgO, Co_3O_4).

S.9.4 Nitrogen isotherm plot for CoZn-MOF-74

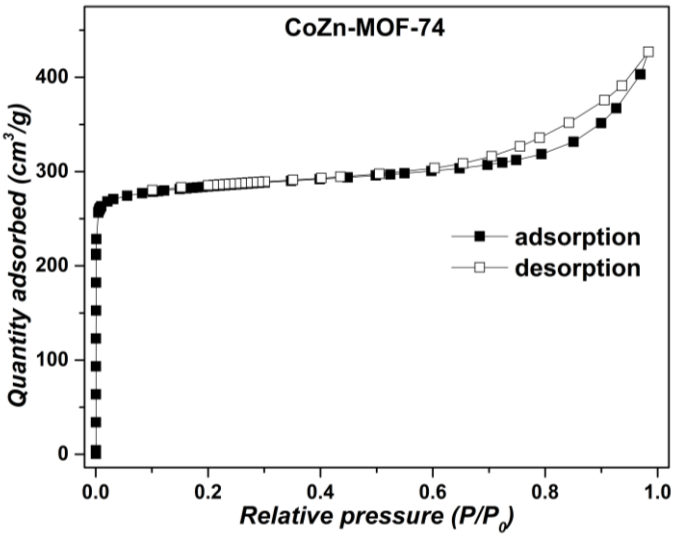

Figure S20. Nitrogen adsorption and desorption isotherms of CoZn-MOF-74.

S.9.5 Nitrogen isotherm plots for CoMg-MOF-74

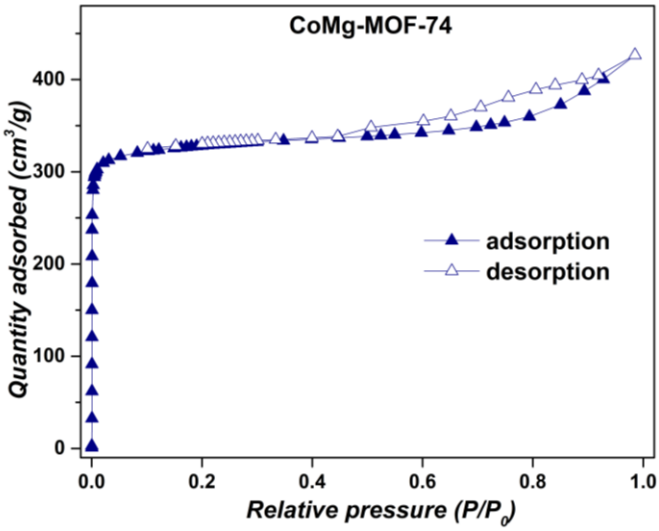

Figure S21. Nitrogen adsorption and desorption isotherms of CoMg-MOF-74.

S.9.6 Nitrogen isotherm plots for CoCu-MOF-74.

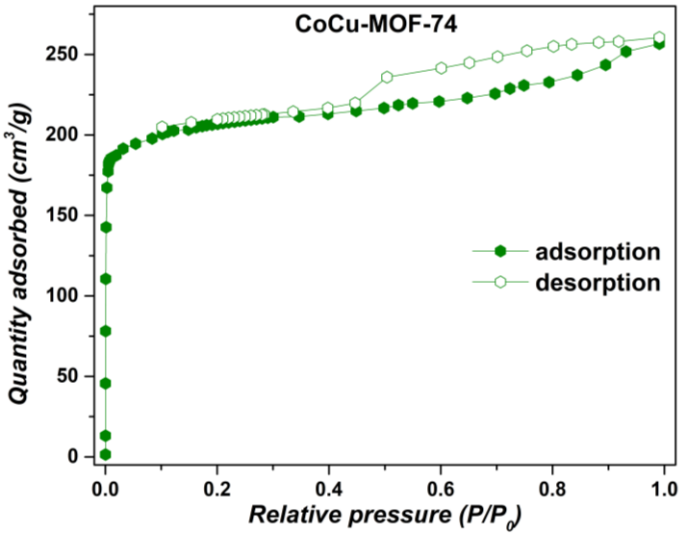

Figure S22. Nitrogen adsorption and desorption isotherms of CoCu-MOF-74.

S.10. Crystallographic information and refinement information for 3

Table S1. Crystal data and structure refinement for **3**.

Empirical formula	$C_8H_{16}NiO_{12}$
Formula weight	362.92
Temperature/K	293(2)
Crystal system	triclinic
Space group	*P*–1
a/Å	6.9497(5)
b/Å	8.6455(5)
c/Å	12.4065(9)
α/°	89.144(5)
β/°	87.701(6)
γ/°	67.707(6)
V/Å^3	689.16(9)
Z	2
ρ_{calc}g/cm^3	1.749
μ/mm^{-1}	2.652
F(000)	376.0
Crystal size/mm^3	0.25 × 0.20 × 0.20
Radiation	CuKα (λ = 1.54184)
2Θ range for data collection/°	7.13 to 133.988
Index ranges	$-7 \le h \le 8$, $-7 \le k \le 10$, $-14 \le l \le 14$
Reflections collected	5148
Independent reflections	2454 [R_{int} = 0.0426, R_{sigma} = 0.0544]
Data/restraints/parameters	2454/18/240
Goodness-of-fit on F^2	1.062
Final *R* indexes [I>=2σ(I)]	R_1 = 0.0494, wR_2 = 0.1289
Final *R* indexes [all data]	R_1 = 0.0548, wR_2 = 0.1355
Largest diff. peak/hole / e Å^{-3}	0.86/–0.57

Table S2. Bond lengths for **3**.

Atom	Atom	Length/Å		Atom	Atom	Length/Å
C11	C13	1.391(4)		C22	O23	1.365(3)
C11	C12	1.405(4)		C22	C23	1.379(4)
C11	C14	1.487(4)		C23	C21[2]	1.400(4)
C12	O13	1.366(3)		C24	O22	1.247(4)
C12	C13[1]	1.380(4)		C24	O21	1.271(3)
C13	C12[1]	1.380(4)		Ni1	O11	2.015(2)
C14	O11	1.251(3)		Ni1	O21	2.0331(18)
C14	O12	1.269(4)		Ni1	O1W	2.0612(19)
C21	C22	1.397(4)		Ni1	O3W	2.066(2)
C21	C23[2]	1.400(4)		Ni1	O4W	2.0786(17)
C21	C24	1.496(3)		Ni1	O2W	2.0972(19)

[1]1–*x*, 2–*y*, 1–*z*; [2]2–*x*, –*y*, 1–*z*

Table S3. Bond angles for **3**.

Atom	Atom	Atom	Angle/°		Atom	Atom	Atom	Angle/°
C13	C11	C12	118.8(3)		O21	C24	C21	115.8(2)
C13	C11	C14	119.6(2)		O11	Ni1	O21	85.61(8)
C12	C11	C14	121.5(2)		O11	Ni1	O1W	89.02(8)
O13	C12	C13[1]	118.7(2)		O21	Ni1	O1W	91.36(8)
O13	C12	C11	120.8(3)		O11	Ni1	O3W	91.46(8)
C13[1]	C12	C11	120.5(3)		O21	Ni1	O3W	92.17(8)
C12[1]	C13	C11	120.7(3)		O1W	Ni1	O3W	176.46(7)
O11	C14	O12	124.0(3)		O11	Ni1	O4W	91.80(8)
O11	C14	C11	117.7(2)		O21	Ni1	O4W	177.32(7)
O12	C14	C11	118.3(3)		O1W	Ni1	O4W	87.92(7)
C22	C21	C23[2]	118.8(2)		O3W	Ni1	O4W	88.55(7)
C22	C21	C24	121.8(2)		O11	Ni1	O2W	176.38(7)
C23[2]	C21	C24	119.4(3)		O21	Ni1	O2W	90.77(7)
O23	C22	C23	117.4(2)		O1W	Ni1	O2W	91.09(7)
O23	C22	C21	122.8(2)		O3W	Ni1	O2W	88.65(7)
C23	C22	C21	119.8(2)		O4W	Ni1	O2W	91.82(7)
C22	C23	C21[2]	121.5(3)		C14	O11	Ni1	131.89(18)
O22	C24	O21	123.4(2)		C24	O21	Ni1	131.86(18)
O22	C24	C21	120.8(2)					

[1]1–*x*, 2–*y*, 1–*z*; [2]2–*x*, –*y*, 1–*z*

S.11 Crystallographic information and refinement information for 4

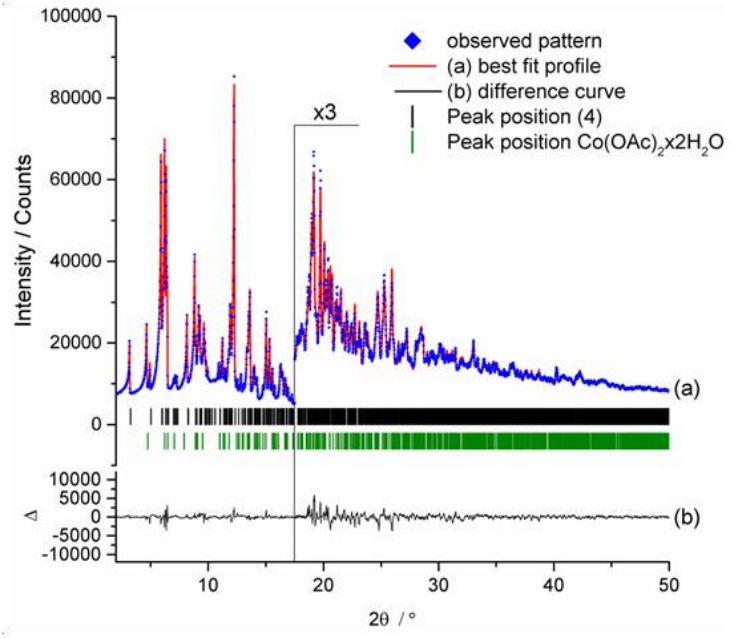

Figure S23. Difference plot for **(4)** with observed intensities (blue squares), calculated intensities (red line), difference curve (black line), calculated peak positions of **(4)** (black bars) and cobalt acetate hydrate (green bars), λ = Cu Kα$_1$.

Table 4. Selected crystal data and details of the Rietveld refinement for **4**.

Compound	$[Co(H_2O)_4(H_2\mathbf{dhta})\cdot 2H_2O]_n$
Formula	$C_8H_{16}CoO_{12}$
MW / g mol^{-1}	363.14
crystal system	*Triclinic*
space group	$P\bar{1}$
Wavelength / Å	*0.7093*
a / Å	6.93886(14)
b / Å	8.6940(2)
c / Å	12.4532(3)
α / °	88.911(2)
β / °	87.481(2)
γ / °	68.358(2)
V / Å^3	697.62(3)
T / K	295
Z	2
D_{calc} / g cm^{-3}	1. 729
μ / mm^{-1}	1.333
No. parameters	39
$2\theta_{max}$ / deg	50
Rwp / %[a]	3.00
Rp / %[a]	2.26
Rexp / %[a]	1.10
RBragg / %[a]	1.36

[a] as defined in TOPAS 5.0

S.12 References

[1] Oxford Diffraction, CrysAlis Software System, Version 1.171.38.46, 2015

[2] (a) Sheldrick, G. M. *Acta Cryst. A*, **2008**, *64*, 112-122. (b) Sheldrick, G. M. SHELXS-2014, Program for Crystal Structure Solution, University of Göttingen, 2014; (c) Sheldrick, G. M. SHELXL, Version 2014/7, Program for Crystal Structure Refinement, University of Göttingen, 2014.

[3] Farrugia, L. J. *J. Appl. Crystallogr.* **1999**, *32*, 837.

[4] (a) Van der Sluis, P. Spek, A. L. *Acta Crystallogr. A*, **1990**, *46*, 194; (b) Spek, A. L. *Acta. Crystallogr.* **2009**, *D65*, 148-155.

[5] Macrae, C. F.; Bruno, I. J.; Chisholm, J. A.; Edgington, P. R.; McCabe, P.; Pidcock, E.; Rodriguez-Monge, L.; Taylor, R.; van de Streek, J.; Wood, P. A. *J Appl Crystallogr*. **2008**, *41*, 466-470.

[6] Bruker A.X.S., TOPAS V5, 2014

[7] Rietveld, H. M. *J. Appl. Cryst.*, **1969**, *2*, 65-71.

[8] R. W. Cheary, A. A. Coelho, J. P. Cline, *J. Res. Nat. Inst. Stand. Tech.*, **2004**, *109*, 1-25.